8-2017

An Upper Limit on the Tightening of Galactic Spiral Arm Pitch Angle in Cosmic Time

Douglas William Shields
University of Arkansas, Fayetteville

An Upper Limit on the Tightening of Galactic Spiral Arm Pitch Angle in Cosmic Time

A dissertation submitted in partial fulfillment
of the requirements for the degree of
Doctor of Philosophy in Physics

by

Douglas W. Shields
University of Houston
Bachelor of Science in Physics, 2001
University of Arkansas
Master of Science in Physics, 2012

August 2017
University of Arkansas

This dissertation is approved for recommendation to the Graduate Council.

Dr. Daniel Kennefick
Thesis Director

Dr. William Harter
Committee Member

Dr. Richard Ulrich
Committee Member

Dr. Claud Lacy
Committee Member

Dr. Reeta Vyas
Committee Member

ABSTRACT

We present Spirality, a novel method of measuring pitch angle by fitting galaxy images to spiral templates of known pitch. Using this algorithm in concert with 2-dimensional Fast Fourier Transform (2DFFT), we determined that the pitch angle of the redshift 2.011 galaxy GZ5001 (J2000 RA 189.14811°, Dec 62.24002°) is approximately $16.2° \pm 2.6°$. The redshift 2.3219 galaxy GS21 (J2000 RA 53.14863°, Dec -27.95469°), which is believed to be the most distant galaxy with visible spiral structure yet measured, has a pitch of approximately $-10.6° \pm 1.6°$. Using a large sample of galaxies from the Great Observatories Origins Deep Survey (GOODS), we place an upper limit on the tightening of average spiral arm pitch angle with cosmic time. With 68% confidence, we find that the average pitch for such galaxies has decreased (tightened) by no more than 9.94 degrees per unit redshift. If we constrain our data to be consistent with the local pitch angle mass function, we find a result that is consistent with a constant average pitch angle over cosmic time.

ACKNOWLEDGEMENTS

The following researchers contributed to this project: M. Shameer Abdeen, Joel C. Berrier, Benjamin Boe, Benjamin L. Davis, William Harter, Matthew Hartley, Daniel Kennefick, Julia Kennefick, Claud H. S. Lacy, Casey L. Pfountz, Hamed Pour-Imani, William Ring, Amanda Schilling, Marc Seigar, and Zac Slade. In addition, I gratefully acknowledge the following individuals and organizations:

- Daniel Kennefick, who took a chance and sponsored my graduate career.
- Claud Lacy, whose lectures inspired me to apply to graduate school.
- Julia Kennefick, who provides counterarguments to keep my science strong and made sure I always got paid.
- William Harter, from whom I once learned something just by strolling by his classroom while he lectured.
- Reeta Vyas, who took time out to help even when it wasn't office hours.
- Rick Ulrich, for welcoming me into a community of like minded space cadets.
- Casey Pfountz and Benjamin Boe, for tirelessly measuring hundreds of pitch angles.
- Amanda Schilling, for asking the tough questions.
- Benjamin Davis, who gave me something to aspire to.
- William Ring, whom I have never met, for pouring through galaxy images and selecting the spirals that would later be used in our sample.

- Ivânio Puerari, for writing the original 2DFFT code on which the later versions of 2DFFT were based.
- Bruce Elmegreen, for helpful comments during private communication.
- The AGES research group, without whom none of this would be possible.
- Rebecca Ragland, who refuses to distinguish between science and art.
- My mother, Lois Ann McIlvain, who told me that picking up litter would be fine profession as long as I had a Ph.D. in it.

This research was funded in part by NSF REU Site Award 1157002. This research has made use of the NASA/IPAC Extragalactic Database (NED) which is operated by the Jet Propulsion Laboratory, California Institute of Technology, under contract with the National Aeronautics and Space Administration. This research has made use of NASA's Astrophysics Data System. This research has made use of the SIMBAD database, operated at CDS, Strasbourg, France. This research made use of Galaxy Zoo.

TABLE OF CONTENTS

LIST OF FIGURES

LIST OF TABLES

LIST OF ABBREVIATIONS

1-D — One-Dimension

2-D — Two-Dimension

2DFFT — Two-Dimensional Fast Fourier Transform

A&A — Astronomy and Astrophysics

A&AS — Astronomy and Astrophysics, Supplement

AAS — American Astronomical Society

AGES — Arkansas Galaxy Evolution Survey

AGN — Active Galactic Nuclei

AJ — Astronomical Journal

Ap&SS — Astrophysics and Space Science

ApJ — Astrophysical Journal

ApJL — Astrophysical Journal, Letters

ApJS — Astrophysical Journal, Supplement

arcsec — Arcsecond ($''$)

ARA&A — Annual Review of Astronomy and Astrophysics

Astron. — Astronomy

Astrophys. — Astrophysics

B-band — Blue light wavelength filter ($\lambda_{eff} = 445$ nm)

B_T — Total apparent B-band apparent magnitude

BH — Black Hole

BHMF — Black Hole Mass Function

CGS — Carnegie-Irvine Galaxy Survey

deg. — Degree (°)

dex — Decimal exponent

DMS — DiskMass Survey

Dr. — Doctor

ed. — Editor

e.g. — exemplī grātiā

Eq. — Equation

ESO — European Southern Observatory

et al. — et alii

etc. — et cetera

Fig. — Figure

FFT — Fast Fourier Transform

GOODS — Great Observatories Origins Deep Survey

H_0 — Hubble constant

H_2O — Water

HST — Hubble Space Telescope

IAU — International Astronomical Union

I-band — Infrared light wavelength filter ($\lambda_{eff} = 806$ nm)

IC — Index Catalogue of Nebulae and Clusters of Stars

i.e. — id est

IFU — Integral Field Unit

IRAF — Image Reduction and Analysis Facility

J. — Journal

km — Kilometer

ΛCDM — Lambda-Cold Dark Matter

log — Base 10 logarithm

M — Messier object

m — Meter

mag — Magnitude

max — Maximum

min — Minimum

MNRAS — Monthly Notices of the Royal Astronomical Society

Mpc — Megaparsec

MSSSO — Mount Stromlo and Siding Spring Observatories

Myr — Megayear

NASA — National Aeronautics and Space Administration

NED — NASA/IPAC Extragalactic Database

NGC — New General Catalogue of Nebulae and Clusters of Stars

NIR — Near-Infrared

nm — Nanometer

No. — Number

NSF — National Science Foundation

ω_b — Physical baryon density

Ω_Λ — Dark energy density

Ω_M — Matter density

PA — Position Angle

PASP — Publications of the Astronomical Society of the Pacific

pc — Parsec

PDF — Probability Density Function

PGC — Principal Galaxies Catalogue

Ph. D. — Doctor of Philosophy

Phys. — Physics

pODI. — partial One Degree Imager

PPak — Pmas fiber PAcK

PSF — Point Spread Function

QLF — Quasar Luminosity Function

r — SDSS red light wavelength filter ($\lambda_{eff} = 623.1$ nm)

R.A. — Right Ascension

R-band — Red light wavelength filter ($\lambda_{eff} = 658$ nm)

RC3 — Third Reference Catalogue of Bright Galaxies

s — Second

SDSS — Sloan Digital Sky Survey

Sgr — Sagittarius

SMBH — Supermassive Black Hole

UK — United Kingdom

Univ. — University

US — United States

V-band — Visual light wavelength filter ($\lambda_{eff} = 551$ nm)

Vol. — Volume

WFPC2 — Wide-Field Planetary Camera 2 on HST

WMAP — Wilkinson Microwave Anisotropy Probe

WP — WMAP Polarization

z — Redshift

1 Introduction

In the local Universe, approximately 60% of large galaxies are disk galaxies with spiral structure (Buta, 1989). Lin & Shu (1964) described spiral arms as long-lived, quasi-stationary density waves that trigger star formation through the compression of gas. In this theory, known as the density wave theory, the spiral pattern rotates more or less rigidly, although the stars and gas do not. Rather, the stars and gas move into the density wave, the gas becomes compressed, (thus triggering star formation), and the stars and gas move out again.

How the density wave pattern remains stable is a topic of ongoing research. A simplistic model involves many particles in slightly eccentric orbits of many different radii, all centered on the galactic center. These orbits precess due to perturbations, with the inner orbits precessing faster than the outer orbits. The orbits therefore "bunch up" into a spiral pattern of overdense material.

The density wave theory explains a number of observed phenomena. The most massive stars (O and B type) have too short a lifespan to escape the density wave before the end of their lives, so they contribute to the luminosity of the spiral arms but not to the interarm region. Moreover, their intense ultraviolet radiation ionizes the surrounding hydrogen, which explains the observed bands of ionized hydrogen (HII) inside spiral arms. Less massive stars with longer lifespans are able to wander out of the spiral arms and populate the interarm region. The least massive stars, including red dwarfs, tend to bunch together on subsequent

passes through the density wave, thus contributing to the luminosity and color gradient between the spiral arm and the interarm medium. Thus, the density wave model has been successful at predicting and explaining the observed rates of star formation and associated ionized gas, the abundance of red dwarfs in the spiral arms, the color gradient at the edge of the arm, and the arm-interarm luminosity contrast.

An alternative model, proposed by Athanassoula et al. (2009a) and Athanassoula et al. (2009b), is called the manifold theory. It relies on the interaction between the stars in the spiral arms and the bar, or elongated bulge, in the galactic center.

According to the manifold theory, spiral arms consist of stars in highly elliptical orbits which are chaotic but nonetheless confined to paths in narrow tubes, or manifolds, the shapes of which are determined by the bar's shape, its size, and the strength of its gravitational potential well. Each star's orbit is highly eccentric and can extend from the edge of the central bar outward to the rim of the galaxy. When the stars fall back into the galactic center, they interact with Lagrange points L1 and L2, which are saddle points at either end of the bar, and L4 and L5, which are unstable points along the sides of the bar. For example, a star may be squeezed into the bar region through L1, herded along the inside of the potential hill formed by L4, and shot back out through L2. By flinging stars outward, the bar drives the formation of spiral arms.

The manifold theory has been successful at explaining some of the more exotic features of barred spirals such as nuclear rings (that is, rings inside the bar), inner rings (those immediately outside the bar) and outer rings (those surrounding the disk). Moreover, the manifold theory has been invoked to explain the peanut-shaped double rings occasionally

seen in galactic disks.

A prediction of the manifold theory is that a galaxy with a stronger gravitational potential in its bar should have a more loosely wound spiral structure. Martínez-García (2012) studied a sample of 27 barred 2-arm spirals which lacked inner rings and whose spirals wound azimuthally for at least 50°. For their entire sample, the manifold theory's prediction seemed to hold, though there was significant scatter in the data. However, when the sample was culled down to the 17 galaxies whose spiral arms wound at least 70°, the scatter was reduced and the trend was more pronounced.

Density wave theory boasts a more robust set of confirmed predictions in terms of stellar populations and ionized gas, and it makes no distinction between barred and unbarred spirals. Manifold theory, on the other hand, has little to say about unbarred spirals, but seems to explain the more exotic subfeatures of barred spirals. At present, it's not clear how much contribution each theory makes to the overall spiral structure of barred galaxies.

The density wave theory has provided a prediction that has proven testable by our research group. In the inner region of the galaxy, the model predicts that stars and gas move faster than the spiral density wave. In the outer region, the stars and gas move more slowly than the spiral pattern. These regions are separated by the corotation radius, at which particles orbit together with the spiral.

Inside the corotation radius, fast-orbiting gas should press into the spiral arm from the back side, triggering star formation on the trailing edge of the wave. Outside the corotation radius, however, the spiral arm's front side should be pushing into the slow-moving gas, triggering star formation on the leading edge of the wave. Thus, the density wave model

predicts that the spiral wave itself, as seen by observing hydrogen gas, should be more tightly wound than the spiral pattern of stars whose birth was triggered by the wave. The present project provides a small contribution toward testing this hypothesis, which will be discussed in more detail later in the Dissertation.

1.1 Pitch Angle

Galactic spiral arms can often, though not always, be reasonably modeled as logarithmic spirals (Seigar & James, 1998). A logarithmic spiral is described by its pitch angle, or tightness of winding, where a spiral with zero pitch would be a circle and a spiral with 90° pitch would consist of radial spokes.

Mathematically, a one-armed logarithmic spiral follows the equation

$$r = r_0 e^{b\theta} \tag{1.1}$$

where r is the radial polar coordinate, θ is the azimuthal polar coordinate, and b is a constant that depends on the pitch angle, ϕ. Following the sign convention of astronomers,

$$b = -tan(\phi). \tag{1.2}$$

The global, best-fit pitch angles of galaxies are an ongoing topic of research because they can be estimated from archival images and correlate with difficult-to-estimate properties such as central black hole mass (Seigar et al., 2008; Berrier et al., 2013) as well as bulge mass and neutral hydrogen density (Davis et al., 2015). Moreover, because of the overabundance

of spiral structure in the local universe compared to the early universe, evolution of spiral structure appears to be an important aspect of galaxy evolution.

Several methods exist of estimating pitch angles, and these methods roughly fall into a few categories: point sampling, one-dimensional Fast Fourier Transforms (1DFFT), two-dimensional Fast Fourier Transforms (2DFFT), and template fitting.

In the point sampling methods, individual points from spiral arms are fit to mathematical spirals, either by a direct least-squares fit (Ma, 2001) or by computing the tangent of the slope on a ln(r) vs. ϕ graph (Kennicutt, 1981). This has the advantage of using minimal, if any, computing power, but also discards potentially useful information by reducing the spiral arms to a set of points that are much less numerous than the pixels in the image.

1DFFT (Grosbol & Patsis, 1998) involves analyzing the azimuthal intensity on circles concentric with the deprojected galaxies. The azimuthal coordinates of the symmetric 2-arm component are plotted vs. the natural log of the radial coordinate, with pitch angle being the resulting slope. Kendall et al. (2011) subtracts out the axisymmetric components in order to enhance the spiral structure before performing 1DFFT on radial bins.

Saraiva Schroeder et al. (1994) described a method of measuring a galaxy's spiral arm pitch angle using a 2-dimensional Fast Fourier Transform (2DFFT). The method measures both the strength and the pitch angle of the various modes (1-arm, 2-arm, etc.) between a given inner radius and a given outer radius. It should be noted that the mode actually describes rotational symmetry rather than the physical number of spiral arms. That is, the 2-arm mode measures the 180-degree symmetric component which usually, though not always, dominates in 2-arm spirals. The resulting pitch is the one that corresponds to the

strongest mode, which hopefully matches the visual number of arms. The weaker modes are generally discarded.

2DFFT methods in general (Saraiva Schroeder et al., 1994; Seigar et al., 2008; Davis et al., 2012; Gonzalez & Graham, 1996; Martínez-García et al., 2014) decompose spiral arms into sums of logarithmic spirals of varying pitches. The number of spiral arms can be stated by the strongest symmetry mode, which allows 3-arm spirals and 4-arm spirals to be analyzed in addition to grand design 2-arm spirals. However, for galaxies with more complex structures such as focculent galaxies, 2DFFT discards asymmetric features that may be of interest to the researcher.

Davis & Hayes (2014) use a sophisticated computer vision algorithm to pick out spiral arm segments, and then models each segment as a logarithmic arc. Each segment may have its own segment length, pitch angle, etc.

In template fitting methods, spiral arms or arm segments are directly matched to spirals of known pitch. Puerari et al. (2014) use template fitting to analyze on individual arms or arm segments, which allows more detailed analysis of spiral structure.

Seigar et al. (2008) used 2DFFT to discover a correlation between a galaxy's spiral arm pitch angle and the mass of its central black hole. Davis et al. (2012) noted that 2DFFT is luminosity-biased, so that the pitch angle near the inner radius is favored in the output. They therefore introduced a variable inner radius to the 2DFFT method. This method shows quantitatively how logarithmic the spiral arms are. It outputs the pitch of the most stable (logarithmic) radius segment. It also establishes error bars by considering the size of the stable radius segment relative to the galaxy radius, as well as the degree to which the stable

segment is logarithmic. Berrier et al. (2013) used the variable inner radius 2DFFT method to tighten the correlation between spiral arms and central black hole mass.

In this dissertation we will introduce Spirality, a MATLAB software which implements a novel algorithm for measuring spiral arm pitch angles that relies on best-fit matching to digital spiral templates. Unlike Davis & Hayes (2014) and Puerari et al. (2014), which analyze local segments of spiral arms, Spirality focuses on the global best-fit pitch.

The Spirality method does not rely on 2DFFT, so it does not force the user to choose a symmetry mode. This is advantageous for galaxies with flocculent (featherlike) spirals and asymmetric spirals. We adopt the variable inner radius method to test for logarithmicity and to establish error bars. We also introduce GenSpiral.m, a code for quickly generating FITS images of synthetic spirals with a wide range of properties. These spirals are useful for testing galaxy measurement and analysis codes.

We also introduce SpiralArmCount.m, a code that uses a one-dimensional Fast Fourier Transform (FFT) to count a galaxy's spiral arms after the pitch angle is determined.

1.2 Evolution of Spiral Arm Pitch Angle

The theory of galaxy formation has become increasingly detailed and sophisticated in recent years, thanks to the relase of high-redshift surveys such as GOODS (Giavalisco et al., 2004), CANDELS (Grogin et al., 2011; Koekemoer et al., 2011), COSMOS (Scoville et al., 2007), GEMS (Caldwell et al., 2008), and HUDF (Beckwith et al., 2006), Galaxy Zoo (Willett et al., 2017; Simmons et al., 2017) and also increased computing power for galaxy simulations.

Spiral galaxies are thought to begin as dense, gas-rich, turbulent disks in which gravitational instabilities pull overdense regions into giant starforming clumps (Elmegreen et al., 2007). The largest clumps fall to the center to become the bulge, and the smallest are moved outward due to angular momentum transport (Elmegreen et al., 2008). Outer clumps may be replenished by infall from cosmological streams (Dekel et al., 2009). The stabilizing effect of the bulge arranges the smaller outer clumps into a "wooly" phase that marks the beginning of spiral structure. As the disk becomes dynamically cool, the remaining clumps dissipate, and gravitational preturbations cause long spiral arms if stars are gravitationally dominant, or flocculence if gas is dominant (Elmegreen & Elmegreen, 2014). Once the bulge is in place, simulations suggest the giant clumps can no longer form (Bournaud & Elmegreen, 2009).

An apparent counterexample to this theory is the $z = 2.18$ galaxy studied by Law et al. (2012), shown in Figure 1.1, which exhibits spiral structure despite being dynamically hot. The authors suggest the observed spiral structure is a short-lived ($\sim$100 Myr) phenomenon sparked by a minor merger. They invoke the short lifespan to explain the rarity of spiral structure in hot disks at $z > 2$.

In this dissertation we will present pitch angle analysis of two additional high-redshift spirals: a one-arm spiral from GOODS South (Giavalisco et al., 2004) with a spectroscopic redshift of $z = 2.3219$, as measured by VLT/VIMOS (Balestra et al., 2010), and an apparent two-arm spiral with a spectroscopic redshift of $z = 2.011$ as measured by (Dawson et al., 2001). The analysis was done by fitting the galaxy to spirals of known pitch using the Spirality software package, and confirmed using variable inner radius 2DFFT (Saraiva Schroeder et al., 1994; Seigar et al., 2008; Davis et al., 2012).

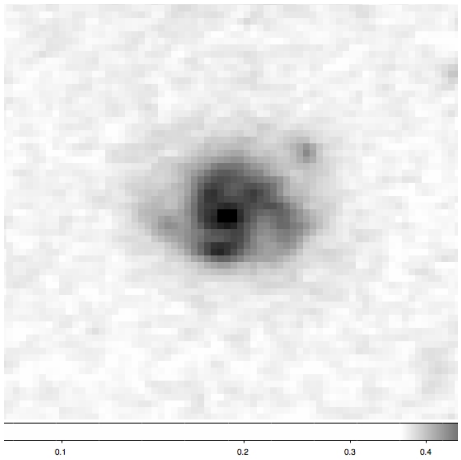

Figure 1.1: Hubble Space Telescope image of Q2343-BX442, the redshift 2.18 spiral described in Law et al. (2012), deprojected from a position angle of 90° and an inclination of 30°.

1.3 Other contributions (Co-author papers)

Before creating the Spirality algorithm, I helped to further develop the technique of measuring pitch angle by two-dimensional Fast Fourier Transform. The technique decomposes images into spirals of varying symmetry modes (numbers of spiral arms) and varying pitch angles, and measures the contribution of each pitch angle to each symmetry mode.

Saraiva Schroeder et al. (1994) developed an early version of this technique based on a routine in *Numerical Recipes in C* (Press et al., 1989). As described in Puerari et al. (2000), the amplitude of each Fourier component with symmetry mode m and pitch angle ϕ is

$$A(p,m) = \frac{1}{D}\int_{-\pi}^{+\pi}\int_{r_{min}}^{r_{max}} I(u,\theta)e^{-i(m\theta+pu)}dud\theta \tag{1.3}$$

where $u \equiv \ln r$, r is the polar radial coordinate, θ is the azimuthal polar coordinates, r_{min} and r_{max} are respectively the inner and the outer radius of the user-defined measurement

annulus, and D is a normalization factor written as

$$D = \int_{-\pi}^{+\pi} \int_{r_{min}}^{r_{max}} I(u,\theta) du d\theta. \tag{1.4}$$

$I(u,\theta)$ is the distribution of pixel values in the (u,θ) plane, m is the harmonic mode (number of symmetrically spaced arms), and p is the variable associated with the pitch angle (ϕ), defined by

$$\tan(\phi) = \frac{-m}{p}. \tag{1.5}$$

The pitch angle of the galaxy, then, is

$$\tan(\phi_{Galaxy}) = \frac{-m}{p_{max}} \tag{1.6}$$

where p_{max} is the value of p with the highest amplitude for a given harmonic mode (see Figure 1.2).

This technique was amended and then used by Seigar et al. (2008) to establish the correlation between spiral arm pitch angle and central black hole mass. The authors found that more massive black holes tend to live in galaxies with more tightly wound spirals, *i.e.* smaller pitch angles. The mass-pitch relation led to the coalescence of the Arkansas Galaxy Evolution Survey, which I then joined.

A disadvantage to the 2DFFT code at the time was that it had no way to estimate uncertainties in its measurements. I was able to contribute to the technique by helping to establish the method by which error bars would be computed.

The code now computes error bars by repeating its computation over many different

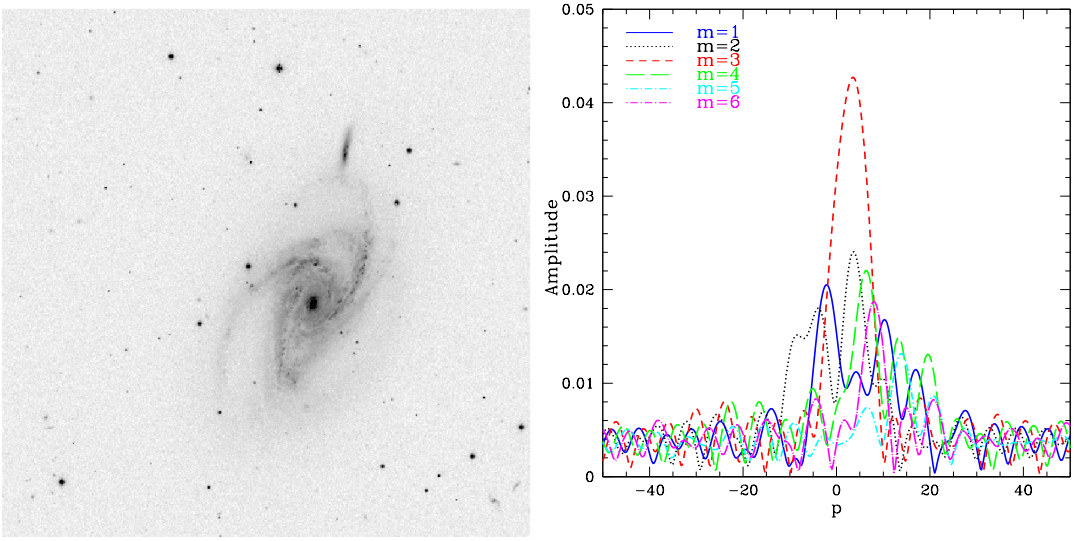

Figure 1.2: **Left:** B-band image of NGC 5054, with position angle 160° and inclination angle 53.84°. **Right:** $A(m, \phi)$ values for a deprojected B-band image of NGC 5054 with a measurement annulus defined by an inner radius of 160 pixels (41.4″) and an outer radius of 508 pixels (132″). The three-arm symmetry of the galaxy is shown by the amplitude peak in the 3-arm mode at $p_{max} = 3.50$, which corresponds to a $-40.60°$ pitch angle according to Equation 1.6. These graph were published in Figure 1 of Davis et al. (2012).

measurement annuli on a single galaxy. The outer radius of all such annuli is the visible rim of the galaxy, while the inner radius varies from the edge of the bulge or bar outward. Because the code is luminosity biased, and most galaxies are brightest in the central regions, 2DFFT tends to weight its measurement toward the inner radius. Thus, by varying the inner radius, we can estimate pitch angle as a function of the radial coordinate.

A logarithmic spiral has a constant pitch. Thus, varying the inner radius gives us a quantitative estimate of how logarithmic the spiral is. Moreover, it gives us a second indicator of the strength of each harmonic mode. If the number of arms is not obvious, we choose the pitch angle of the mode with the highest amplitude and the most logarithmic (that is, constant with radius) pitch.

Quantitatively, the degree of logarithmicity contributes to the error bar in two ways.

First, the user chooses a range of radial coordinates with nearly constant pitch, hereafter called the "stable region". The mean of the pitch angles measured on their respective inner radii in the stable region is output as the pitch angle of the galaxy. The standard deviation of the pitch angles measured on their respective inner radii in the stable region is computed as a first-order error estimate.

In addition to the standard deviation of the pitch angles in the stable region, we must also take into account the size of the stable region compared to the radius if the galaxy. If the stable region spans the radius of the galaxy, then the uncertainty is minimized. However, this is rarely the case. We therefore scale the first-order error estimate by the ratio of the galaxy radius to the size of the stable region. A long stable region indicates a nearly logarithmic spiral. A small stable region receives a large error bar because it indicates a spiral that deviates significantly from logarithmicity. We refer to this scaled error estimate as the "stretched error".

There is another source of uncertainty in 2DFFT measurements that is independent of the galaxy properties. The code is only able to output the variable p in discrete steps. Therefore, when p is used to compute the pitch angle, only discrete values of pitch angles are allowed to be computed. Since the range of possible results is quantized rather than continuous, there is an error associated with the computation. We refer to this as the "quantized error", or the difference between the output pitch angle and the next highest pitch angle which the code is able to produce.

The quantized error increases with pitch angle and decreases with harmonic mode. In our galaxy samples, pitch angles rarely exceed 40° and the number of arms is usually 2

or more. Given these values, the quantized error can be as much as 3°, but is usually 1° or less.

The overall uncertainty of the pitch angle measurement, then, combines the contributions from the stretched error and the quantized error:

$$E_\phi = \sqrt{(\beta\sigma/\lambda)^2 + \epsilon_m^2} \tag{1.7}$$

where E_ϕ is the total pitch angle error, ϵ_m is the quantized error for the dominant harmonic mode, σ is the standard deviation about the mean pitch angle, β is the distance in pixels from the innermost stable spiral structure (i.e., beyond the influence of a bulge or bar) to 90% of the selected outer radius of the galaxy ($0.9r_{max}$), and λ is the length in pixels of the stable range of radii over which the pitch angle is averaged.

Figure 1.3 illustrates the variable inner radius method. The results are published in Davis et al. (2012), in which we describe our updated 2DFFT code.

We used the updated computation method to retest the mass-pitch relation, and found a tighter correlation than was previously published. The new relation is given by

$$log\left(\frac{M}{M_\odot}\right) = 8.21 - 0.062|\phi| \tag{1.8}$$

where M is the black hole mass, $M_\odot$ is the solar mass, and ϕ is the spiral arm pitch angle in degrees. Note that the absolute value simply means that we did not take into account the chirality, or direction of winding. The slope has an error of 0.009 inverse degrees, and the intercept has an error of 0.16. The result is published in Berrier et al. (2013).

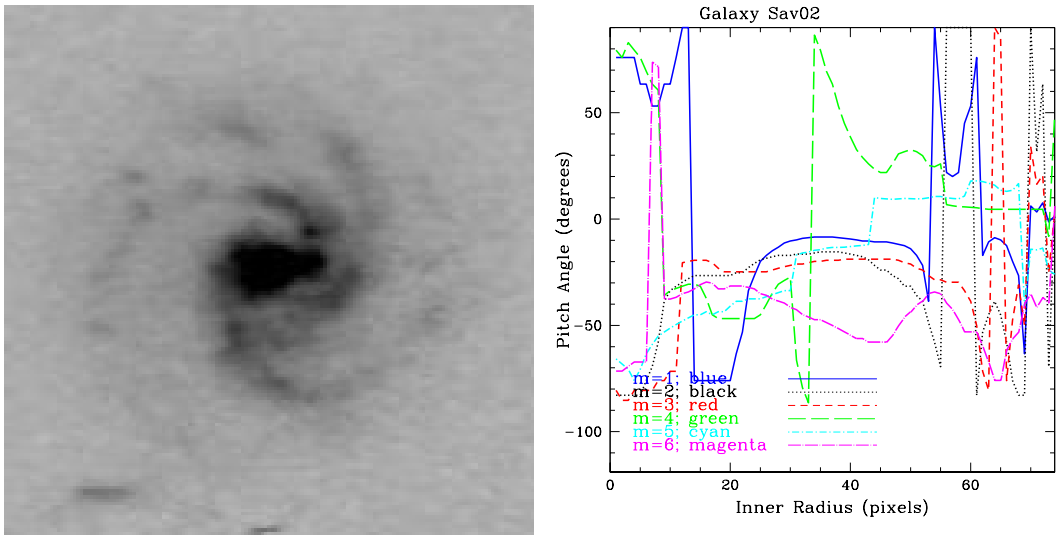

Figure 1.3: **Left:** A three-arm galaxy from Hubble Ultra Deep Field at J2000 coordinates RA 3h 32m 39.26s, Dec -27° 45' 32.73". **Right:** Pitch angle vs. the inner radius of the measurement annulus for this galaxy. For the 3-arm mode, the stable region is between 13 and 53 pixels, while the galaxy radius is 75 pixels. Within that region, the mean pitch is -21.42°, with the negative sign denoting Z-winding. The standard deviation of pitches within the stable region is 2.41°. The stretched error, which is the standard deviation scaled by the ratio of the galaxy to the size of the stable region, is 4.52°. The quantized error, which is an artifact of the computation method which depends on the mean pitch and the harmonic mode (in this case, 3), is 1.42°. The total error is the stretched error added in quadrature to the quantized error, or 4.67°.

Once a tighter correlation was established between pitch angle and black hole mass, we were able to determine the local black hole mass function, which is a census of black hole masses in the local Universe.

In order to ensure completeness in our sample, *i.e.* that our sample is representative of the population of galaxies within the stated parameters, we chose to construct a volume-limited sample of galaxies. A volume-limited sample which consists of all the galaxies within a certain volume that are brighter than a certain apparent magnitude, or apparent brightness.

In addition to measuring some of the pitch angles, my contribution to this project was to construct the volume-limited sample. I began with the *Carnegie-Irvine Galaxy Survey*,

or CGS (Ho et al., 2011). This sample is magnitude-limited, consisting all 605 galaxies in the southern celestial hemisphere with apparent magnitude brighter than 12.9 in the 445-nm blue band ($B_T > 12.9$). After rejecting all galaxies except spirals and adding the Milky Way to our sample, we were left with 385 magnitude-limited galaxies.

The left panel of Figure 1.4 shows the absolute magnitude (a logarithmic luminosity scale) in the B band versus luminosity (redshift-independent) distance for all 385 magnitude-limited spirals. The distances were taken from the *NASA/IPAC Extragalactic Database*, or NED. The solid curve is the visually determined magnitude limit. In other words, galaxies above the line appear too dim to be included in the magnitude-limited sample. For the local Universe, the curve is an exponential.

In order to extract a complete, volume-limited sample from a magnitude-limited sample, it is necessary to choose both a minimum luminosity and a maximum distance. These quantities must be chosen such that a galaxy at the maximum distance and minimum luminosity appears bright enough in our sky to be included in the original magnitude-limited sample. In other words, the two quantities are not independent. The larger the maximum distance, the brighter the galaxies must be (that is, the lower the absolute magnitude).

There are many such combinations of maximum distance and minimum luminosity. On a graph of absolute magnitude versus distance for a magnitude-limited sample, a volume-limited sample consists of all the galaxies inside a rectangle whose diagonal connects the origin to any point on the magnitude cutoff curve.

In the left panel of Figure 1.4, the dashed lines contain the volume-limited subsample we chose. The vertical line shows the subsample's maximum distance of 25.4 Mpc, while the

horizontal shows the maximum absolute B-band magnitude (corresponding to a minimum luminosity) of -19.2223.

We chose this combination of maximum distance and maximum absolute magnitude in order to maximize the number of galaxies in our volume-limited subsample. The right panel of Figure 1.4 shows the number of galaxies in 100,000 possible volume-limited subsamples as a function of maximum distance. The curve peaks at 25.4 Mpc, which is why we chose that value.

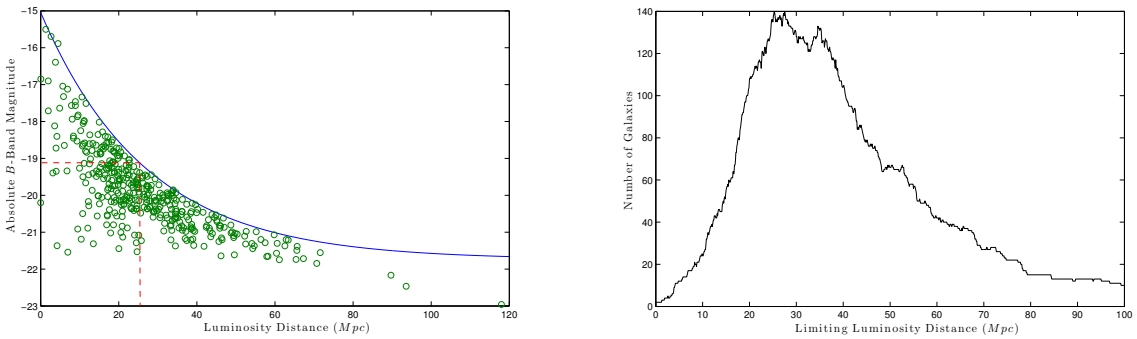

Figure 1.4: **Left:** luminosity distance vs. absolute B-band magnitude for all 385 spiral galaxies in the Southern hemisphere with apparent B-band magnitudes brighter than 12.9. The upper limit absolute magnitude can be modeled as an exponential and is plotted here as the solid line. The dashed rectangle is constructed to maximize the number of galaxies in the volume-limited sample. The limiting luminosity distance and absolute B-band magnitude are set to be 25.4 Mpc and -19.12, respectively. **Right:** histogram showing the number of galaxies contained in the box in the top panel as the box is allowed to slide to new positions based on the limiting luminosity distance. Note there is a double peak in the histogram maximizing the sample each at 140 galaxies. The two possible combinations are $D = 25.4$ Mpc and $M_B = -19.12$ or $D = 27.6$ Mpc and $M_B = -19.33$. We chose to use the former (leftmost peak) because its volume-limiting sample is complete for galaxies with dimmer intrinsic brightness. In total, the two samples differed by only 20 non-mutual galaxies, a difference of $\approx 14\%$. Complete volume-limited samples were computed for limiting luminosity distances ranging from 0.001 Mpc to 100.000 Mpc in increments of 0.001 Mpc. These graphs were published in Davis et al. (2014).

Some galaxies had to be rejected from the volume-limited sample because their inclination angle was too close to edge-on to take a good pitch angle measurement. The final

sample consisted of 128 galaxies.

Given our complete volume-limited sample of all 140 spiral galaxies in the Southern hemisphere within a distance of 25.4 Mpc, absolute B-band magnitudes brighter than -19.12, and inclination angles sufficiently face-on to take good measurements, we were able to determine a local pitch angle function.

My contribution to the pitch angle distribution calculation was to solve the problem of formulating a statistical distribution from data points with differing uncertainties. The solution was to model each data point (that is, each galaxy's pitch angle measurement) as a Gaussian distribution. The pitch angle itself was the mean, and the uncertainty was the standard deviation. All 140 Gaussian functions were added together, and the resulting curve was normalized. The resulting "binless histogram" is shown in the left panel of Figure 1.5.

The dashed line shows the binless histogram itself, while the solid line shows the smoothed distribution, modeled as a Type IV Pearson probability density function with the same mean, standard deviation, skewness, and kurtosis as the binless historgram. These statistics were computed by creating 1,000 artificial data points for each galaxy. Each galaxy's artificial data points consisted of random, normally distributed pitch angles for which the mean was the galaxy's pitch angle and the standard deviation was the uncertainty. The process of computing 1,000 data points for each of 128 galaxies gave us 128,000 data points which were now evenly weighted. From those data points, we computed the aforementioned Pearson statistics.

The result was a peak (that is, most probable in a random sample) pitch angle of 18.52° for the local Universe. The mean pitch angle was 21.44° with a standard deviation of

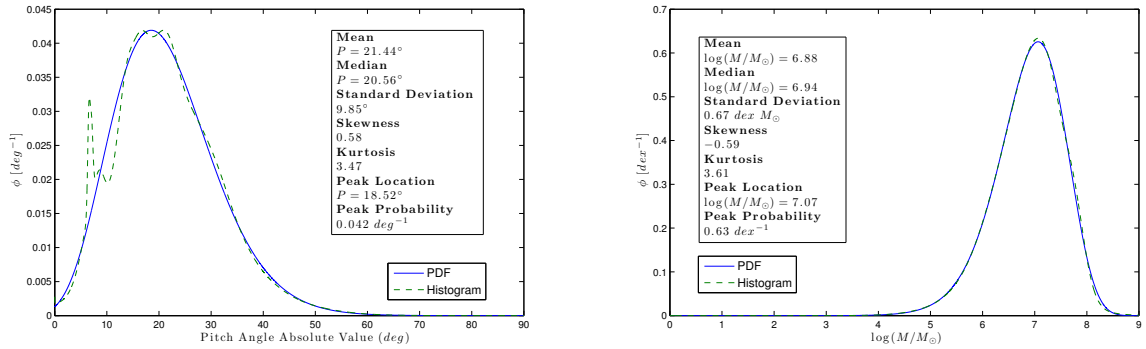

Figure 1.5: **Left:** Pitch angle distribution (dashed) and best-fit Pearson probability density function (solid) fit to the data, as published in Davis et al. (2014). The pitch angle distribution is a "binless" histogram that we modeled by allowing each data point to be a Gaussian, where the pitch angle absolute value is the mean and the error bar is the standard deviation. The pitch angle distribution is then the normalized sum of all the Gaussians. The resulting PDF has mean 21.44°, standard deviation 9.85°, skewness of 0.58, and kurtosis 3.47. The peak probability is 18.52°, with a probability density of 0.042 degree^{-1}. **Right:** Black hole mass distribution (dashed) and best-fit Pearson probability density function (solid) fit to the data. The black hole mass distribution is a "binless" histogram that we modeled by allowing each data point to be a Gaussian, where the black hole mass is the mean and the error bar is the standard deviation. The black hole mass distribution is then the normalized sum of all the Gaussians. The resulting PDF has a mean of 6.88 dex $M_\odot$, standard deviation 0.67 dex $M_\odot$, skewness -0.59, kurtosis 3.61, and a most probable SMBH mass of $\log(M/M_\odot) = 7.07$ with a probability density value of 0.63 per dex.

9.85°, a skewness of 0.58, and a kurtosis of 3.47.

From that distribution, the paper's first author Ben Davis calculated a local black hole mass function based on the relationship found in Seigar et al. (2008) and revised in Berrier et al. (2013). The result is shown in the right panel of Figure 1.5. As in the left panel, the dotted line represents a binless histogram and the solid line represents a Pearson probability distribution function.

The resulting black hole mass function has a peak black hole mass of $10^{7.07}$ solar masses. The horizontal axis in the right panel of Figure 1.5 shows the common logarithm of black hole mass in solar masses. The mean is 6.88 with a standard deviation of 0.67, a

skewness of -0.59, and a kurtosis of 3.61.

These results were published in Davis et al. (2014).

1.4 Distant galaxies and the Spirality algorithm

The next step was to study the evolution of spiral arm pitch angle in cosmic time, and from that result, to glean preliminary insights about the evolution of black hole mass. Such insight is preliminary until it can be established whether the mass-pitch relation itself evolves.

An obvious sample for this project was the Great Observatories Origins Deep Survey (GOODS) (Giavalisco et al., 2004). This survey is a multi-wavelength collection of images from Hubble Space Telescope, Chandra X-ray Observatory, and other large telescopes, all observing the same patch of sky with long exposure times.

We used a sample of visually selected spirals from Hubble Deep Field North and Chandra Deep Field South, with distances out to a redshift of 2.5, which corresponds to a distance of about 11 billion light-years. Many of the images were extremely low-resolution, and some of the galaxies' angular radii were less than 25 pixels.

Not surprisingly, 2DFFT had difficulty measuring some of these galaxies. Some of the difficulties were expressed quantitatively as the code output large error bars. However, I intuited that 2DFFT was overconfident in some of its measurements. I therefore wanted to create an independent algorithm to serve as a check on 2DFFT. That way, we could maintain a subsample of distant, low-resolution galaxies for which independent measurement methods agreed on the pitch angle result.

The resulting algorithm is called Spirality. In addition to analyzing the evolution of pitch angle in the GOODS field, it was used by Pour-Imani et al. (2016) to measure pitch angles of local galaxies in varying wavelengths. These papers establish the existence of corotation radii in local galaxies. The results serves as a theory test; they favor the density wave model over the swing amplification model.

In this dissertation we discuss the Spirality algorithm and the scientific results it has produced. In Chapter 2 we describe the Spirality algorithm in detail. In Chapter 3 we analyze spiral structure in a galaxy beyond redshift 2. Galaxies at this distance rarely show spiral structure, and this particular galaxy may be the most distant galaxy with visible spirals yet studied. In Chapter 4 we place an upper limit on the evolution of spiral arm pitch angle with cosmic time.

2 Spirality: A Novel Way to Measure Spiral Arm Pitch Angle

We present the MATLAB code Spirality, a novel method for measuring spiral arm pitch angles by fitting galaxy images to spiral templates of known pitch. Computation time is typically on the order of a minute per galaxy, assuming at least 8 GB of working memory. We tested the code using 117 synthetic spiral images with known pitches, varying both the spiral properties and the input parameters. The code yielded correct results for all synthetic spirals with galaxy-like properties. We also compared the code's results to two-dimensional Fast Fourier Transform (2DFFT) measurements for the sample of nearby galaxies defined by DMS PPak. Spirality's error bars overlapped 2DFFT's error bars for 26 of the 30 galaxies. The two methods' agreement correlates strongly with galaxy radius in pixels and also with i-band magnitude, but not with redshift, a result that is consistent with at least some galaxies' spiral structure being fully formed by $z = 1.2$, beyond which there are few galaxies in our sample. The Spirality code package also includes GenSpiral, which produces FITS images of synthetic spirals, and SpiralArmCount, which uses a one-dimensional Fast Fourier Transform to count the spiral arms of a galaxy after its pitch is determined.

2.1 Introduction

A major aim in developing Spirality is for use in theory testing. The underlying physical causes of spiral arm structure in disk galaxies is still debated, and it seems appropriate to seek out ways in which measurement can decide between competing theories. Spirality

is capable of quantifying two important aspects of spiral arm structure: It can measure the pitch angle of the arms without assuming rotational symmetry, and it can count the number of arms.

The two main versions of density wave theory, the modal theory and the swing amplification theory, suggest that young stars born in the spiral arms should move ahead of the density wave in the inner disk but fall behind in the outer disk, due to differential rotation. The result is that the star-forming dust (far infrared) and the short-lived massive stars (far ultraviolet) should be more loosely wound than the older, longer-lived stars (optical and near-infrared) (Grosbol & Patsis, 1998). The manifold theory, on the other hand, suggests that pitch angle should be independent of wavelength (Athanassoula et al., 2010).

Pour Imani et al. (2016) showed that for a sample of 16 galaxies, the pitch angle in the far ultraviolet (151 nm) is the same as the pitch angle in the far infrared (8.0 μm), and both of these pitches are systematically looser than the pitches in the optical and near-optical bands. This result strongly favors the modal density wave theory and the swing amplification theory over the manifold theory.

In order to discriminate between the modal density wave theory and the swing amplification theory, it is necessary to look more closely at their respective predictions. Berrier & Sellwood (2015) and D'Onghia (2015) observed that swing amplification demands that a denser disk cannot support multiple armed modes, with m>3. In general, there should be a correlation between number of spiral arms and the density of the disk. We seek to investigate these claims using SpiralArmCount, a part of Spirality package which can count a galaxy's arms in a simple and robust way which is probably superior to that of 2dFFT, which itself

is actually well suited to this task.

Another theory-testing application involves the question of when spiral arms first formed. Elmegreen & Elmegreen (2014) report that spiral structure began at around z $\sim$ 1.8. Such high-redshift galaxies are often viewed as low-resolution images, so it is useful to have at least two independent methods of estimating pitch angle, such as 2DFFT and a template fitting method such as Spirality.

Spirality has two main advantages. First, as will be shown, the pitch angle result describes the entirety of the galaxy in the measurement annulus, rather than stating only the dominant symmetry mode. Second, Spirality provides a clear way to count the spiral arms without assuming rotational symmetry.

2.2 Spiral Coordinate System

A spiral's pitch angle P is the angle between the spiral's tangent line and a concentric circle's tangent line. For a logarithmic spiral, P is constant, though for a physical spiral (*e.g.* a galaxy), the pitch may vary from arm segment to arm segment.

A real orthogonal coordinate system with logarithmic spiral axes can be constructed. One set of axes has pitch angle P, where $-90° \leq P \leq 90°$. The orthogonal axes (which our computation method disregards) has pitch angle $P' = P \pm 90°$, where $-90° \leq P' \leq 90°$.

In order to construct one of the spiral coordinate axes, let a one-arm spiral be given by

$$r = e^{b\theta} \tag{2.1}$$

where r is the radial polar coordinate, θ is the azimuthal polar coordinate, and b is the

so-called spiral constant.

The pitch angle, using the sign convention of astronomers, is then given by the spiral constant b in equation 2.1:

$$P = \tan^{-1}(-b) \tag{2.2}$$

The arclength S along the spiral from the origin to some outer radius R is given by

$$S = \left| R\frac{\sqrt{1+b^2}}{b} \right| \tag{2.3}$$

The spiral coordinate system then consists of many one-arm spirals, each given by

$$r = e^{b[\theta-\theta_0]} \tag{2.4}$$

Each axis has a unique phase angle θ_0, such that $0 \leq \theta_0 < 2\pi$.

The orthogonal set of axes is not computed for our purposes.

2.3 Computation Method

Our method finds a galaxy's best-fit pitch angle by matching the deprojected galaxy to a set of spiral coordinate systems (templates) with known pitch angles. The first step is to create a single template.

The Cartesian pixel coordinates are recorded along each spiral axis. We establish a set of evenly spaced points along the first spiral axis for the purpose of recording pixel values. The axis points are spaced sufficiently close together so that a single pixel may be recorded several times. The longer the path of the axis through a given pixel, the more times the

pixel is counted. The mean pixel value along the axis is then recorded.

Figure 2.1 illustrates the process of finding the mean pixel value along a given spiral axis. The distance in pixels between the sampling points is called AxisPointSpacing, and is an input parameter that can be adjusted if computation time becomes an issue.

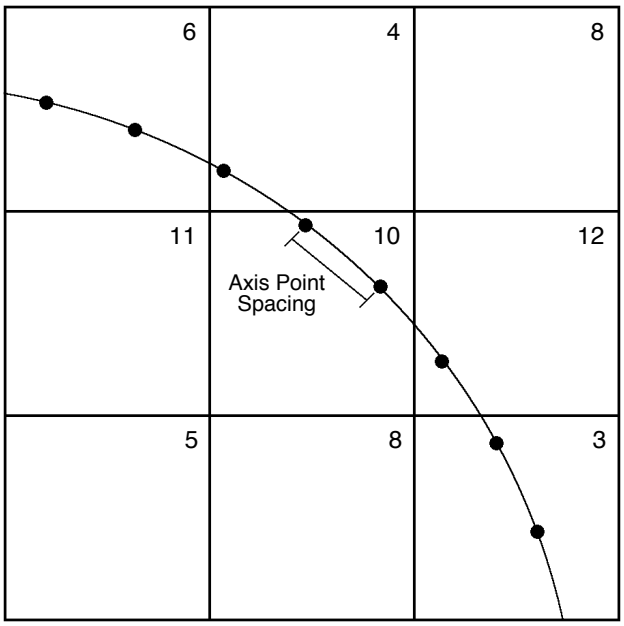

Figure 2.1: Illustration for computing the mean pixel value on a given spiral axis with a given pitch. The squares represent pixels on a galaxy image, and the numbers are the pixel values. The solid curve represents one spiral axis; the dots are the sampling points. The AxisPointSpacing input parameter is the distance, in pixels, between sampling points. The mean pixel value is the mean of all the pixels cut by the spiral, weighted by the number of sampling points in each pixel. For the spiral axis segment shown in this figure, the mean pixel value is (2*6 + 4 + 2*10 + 12 + 2*3)/8 = 6.75. The variance of these means, computed over all spiral axes for a given pitch angle, yields the fitting function for that pitch. When the axis pitch most closely matches the galaxy's pitch, the fitting function is maximized.

The process is repeated for the remaining axes. The number of axes is chosen by the user; we recommend $4\pi R$, where R is the galaxy radius in pixels, so that the pixels at the outer edge of the measurement annulus get read, on average, twice.

Once the mean pixel value for each spiral axis is recorded in the first template, the variance of these means is computed. This is the fitting function. Its value is assigned to the pitch angle of the template. The process is then repeated for templates of many different pitches, resulting in the fitting function (variance of means) vs. template pitch angle.

If the code is measuring a synthetic spiral or a particularly clean galaxy image, the fitting function shows a global maximum at the spiral's true pitch. However, the presence of even a single foreground star can produce a monotonically increasing background in the fitting function. The true pitch may therefore produce a local maximum, with the global maximum occurring at the edge of the graph. Visual inspection of the graphs is therefore required.

2.3.1 Error Bars

Error bars are determined in a manner similar to Davis et al. (2012). The pitch angle is measured on a series of annuli that are concentric with the galaxy. The outer radius is held constant, while the inner radius is varied. The fitting function now spans two independent variables: template pitch angle and inner radius.

A region of inner radii with reasonably constant pitch is identified by the user, and the standard deviation of the pitches in this region is computed. This number is scaled by the size of the stable radius segment relative to the radius of the galaxy. The result is added in quadrature with the measurement precision, or the number of degrees between consecutive template pitch angles. The error bar is output.

Because the error bar is larger if the logarithmic segment of the galaxy radius is smaller, the error bar is a first-order test of logarithmicity. If the user either overestimates

or underestimates the length of the logarithmically stable radius segment, the error bar will suffer.

The measurement's precision, in degrees, is chosen by the user. We have found it useful to measure each galaxy twice. The first measurement is coarse (poor precision) but spans a wide domain of template pitch angles. The true pitch is visually estimated as a local maximum in the fitting function. Since the code outputs the global maximum, the output pitch may represent the edge of the graph rather than the true pitch. The galaxy is therefore remeasured with fine precision, spanning a narrow pitch angle domain in the region of the true pitch. On this domain, the true pitch is the global maximum, and is therefore output.

2.3.2 Measuring a Symmetric Component

For galaxies that are particularly noisy, riddled with foreground stars, or for some other reason difficult to measure, the code package includes SymPart.m, which returns the galaxy's 2-arm (180° rotational) component. Computation time for SymPart is negligible. The method is to pair each pixel with the pixel that is symmetric to it about the origin. The brighter of the pair is then reduced in value to the dimmer.

Measuring the pitch angle of the 2-arm component (mode) sometimes yields a more decisive answer than the galaxy as a whole. Moreover, if the image is not star subtracted, taking the symmetric component can be a quick way to eliminate most foreground stars. The disadvantage of taking the symmetric component is that it assumes 2-arm symmetry, while disregarding all information to the contrary.

SymPart can also yield the 3-arm component, by grouping each pixel with two other pixels at the same radial coordinate. The three grouped pixels form an equilateral triangle

about the origin. The brightest two pixels in the group are reduced in value to the dimmest pixel. Using a similar method, the 4-arm component can also be taken.

In order to test SymPart, we added the resulting symmetric component to its residuals in hopes of recovering the original galaxy. The tests were successful for the 2-arm, 3-arm, and 4-arm components, but not for higher modes. We do not recommend using SymPart for modes higher than 4.

2.3.3 Measuring a Combination of Symmetric Components

For galaxies with only one or two foreground stars, the code package includes MultiSymPart.m, which quickly returns a combination of the 2-arm and 3-arm components. Computation time for MultiSymPart is negligible. The method is to compute the 2-arm component as described above, then compute the 3-arm component of the residual, and then add the two results. This can often eliminate a foreground star or two while disregarding only as much information as is necessary. The user can also include the 4-arm component.

As with SymPart, we tested MultiSymPart by adding the output to the final residuals in hopes of recovering the original galaxy. We do not recommend using MultiSymPart for modes higher than 4.

2.3.4 Counting the Spiral Arms

Once the pitch angle of a galaxy has been determined, the code package includes SpiralArmCount.m for counting the spiral arms. This code is useful for showing quantitatively whether or not a galaxy has an integer number of arms, particularly when a simple visual

inspection of the galaxy gives an ambiguous answer. Computation time for SpiralArmCount is negligible.

SpiralArmCount requires the pitch angle as an input. The user can use either Spirality or any other method to determine the pitch angle.

The method is to analyze the image using a spiral coordinate system with the same pitch angle as the galaxy. The median pixel value V_{med} is computed along each spiral axis. A graph of V_{med} vs. coordinate axis phase angle θ_0, where $0 \leq \theta_0 < 2\pi$, is available for the user's inspection.

The counting function is the FFT of V_{med} vs. θ_0. The resulting domain frequencies are converted to modes (1-arm, 2-arm, etc.), and the number of spiral arms is represented by the strongest mode.

Like 2DFFT, Spirality's SpiralArmCount function uses an FFT as its counting function. As with all FFT's, there are some quirks.

First, the 1-arm mode analyzes a wavelength that spans the entire data set, which limits FFT's precision. The 1-arm mode for both Spirality and 2DFFT should therefore be eyed with caution.

Second, because SpiralArmCount relies on a Fast Fourier Transform, it does not, strictly speaking, count the arms. Rather, it is a statement of symmetry. Therefore, a three-arm galaxy with two bright, 180° symmetric arms and one dimmer, asymmetric arm will appear to both 2DFFT and to Spirality's SpiralArmCount function as a 2-arm galaxy because of its 2-arm symmetry. The advantage of SpiralArmCount is that, in addition to the FFT, it also produces a graph of median pixel value vs. axis phase angle. On this graph,

each spiral arm is represented by a local maximum. This gives the user a way to count the spiral arms independently of both the galaxy image and the FFT. The graph also provides a visual representation of the arm-interarm contrast, an ongoing topic of study (Gonzalez & Graham, 1996).

Figure 2.2 shows the counting function for a 2-arm galaxy with symmetrically spaced arms, 3-arm galaxy with symmetrically spaced arms, and a 3-arm galaxy with two 180° symmetric arms and one asymmetric arm. Note that SpiralArmCount sees the 3-arm galaxy with $m = 2$ symmetry as a 2-arm spiral.

SpiralArmCount also outputs a .fits image of the original galaxy, annotated with the spiral axes at phase angles 0 and $\pi/2$ radians. This allows the user to associate each peak in the counting function with its corresponding spiral arm. Unlike in Figure 2.2, SpiralArmCount does not label the two axes. Rather, the zero axis is both wider and brighter (*i.e.*, has higher pixel values) than the $\pi/2$ axis.

2.4 Pitch Angle Measurement Examples

2.4.1 Synthetic Spiral

Figure 2.3 shows Spirality's measurement of a synthetic two-arm spiral of radius 100 pixels, arm thickness 3 pixels, and pitch angle 20°. The inner radius of the measurement annulus varied from 5 pixels to 65 pixels in steps of 10 pixels. The outer radius remained constant at 98 pixels. Using the variable inner radius method to establish error bars, the resulting pitch is $19.97° \pm 0.13°$.

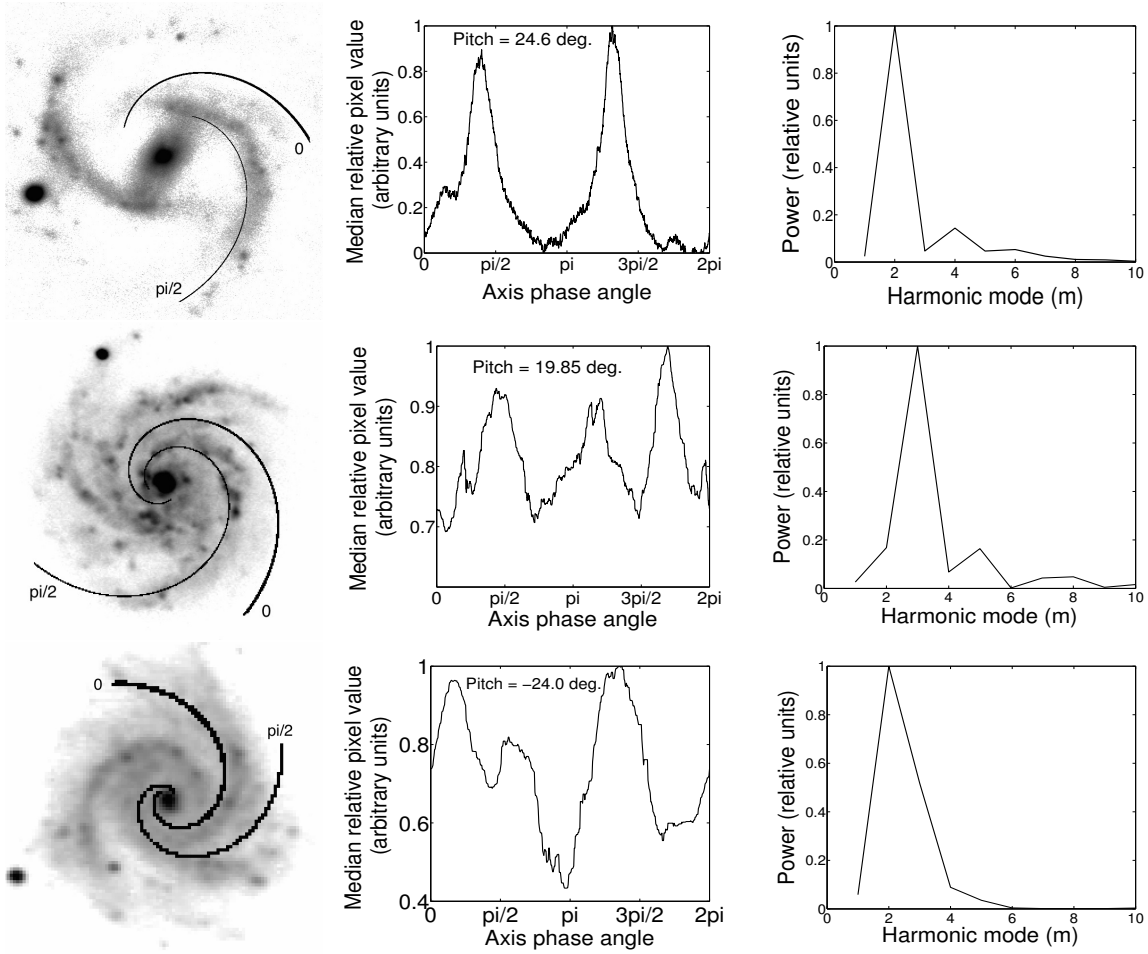

Figure 2.2: SpiralArmCount's outputs of UGC 1081 with two symmetrically spaced arms (**top row**), UGC 463 with three symmetrically spaced arms (**middle row**), and UGC 4107 with two bright arms approximately 180° apart and a third, slightly smaller arm (**bottom row**). The **left column** shows each galaxy image, annotated with the spiral axes at respective phase angles 0 and $\pi/2$ radians. The **middle column** shows the median pixel value along each spiral axis, where the spiral coordinate system has the same pitch as the galaxy. Each local maximum represents a spiral arm. The **right column** shows the counting function. It is the FFT of the middle column, except the frequency axis is converted to harmonic modes. All images were deprojected to face-on prior to analysis.

2.4.2 Simple Galaxy: UGC 463

Figure 2.4 shows Spirality's measurement of galaxy UGC 463. This B-band image was taken with the 2.1-meter telescope at Kitt Peak National Observatory. The inner radius of the measurement annulus varied from 0 to 45 pixels. Under normal circumstances, the

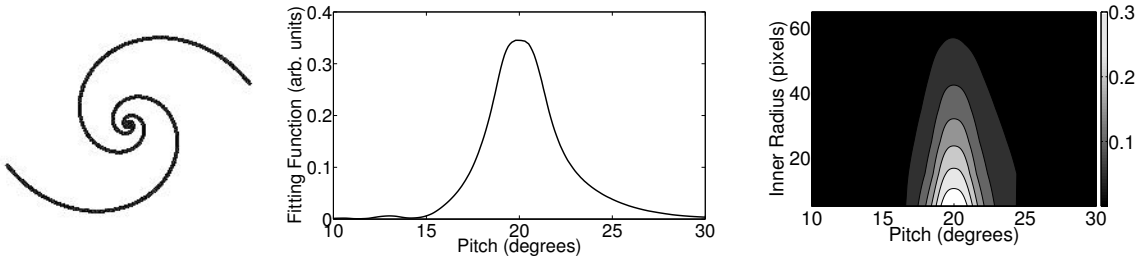

Figure 2.3: Spirality's measurement of the synthetic two-arm spiral of pitch angle 20°, shown in the **left panel**. **Center:** Fitting function vs. pitch angle for a measurement annulus with inner radius 5 pixels, or 5% of the outer radius. The outer radius of the measurement annulus is approximately equal to the outer radius of the spiral. **Right:** Fitting function vs. pitch angle and measurement annulus inner radius. Note that the center panel is a cross section of the right panel. Spirality's measurement gives a best-fit pitch of $19.97° \pm 0.13°$.

outer radius would be placed at the visible edge of the spiral arms. However, this image contains a foreground star near the edge of the galaxy. In order to prevent Spirality from interpreting the star as part of a spiral arm, the outer edge of the measurement annulus was placed just inside the star's radial position. Spirality therefore did not see the star.

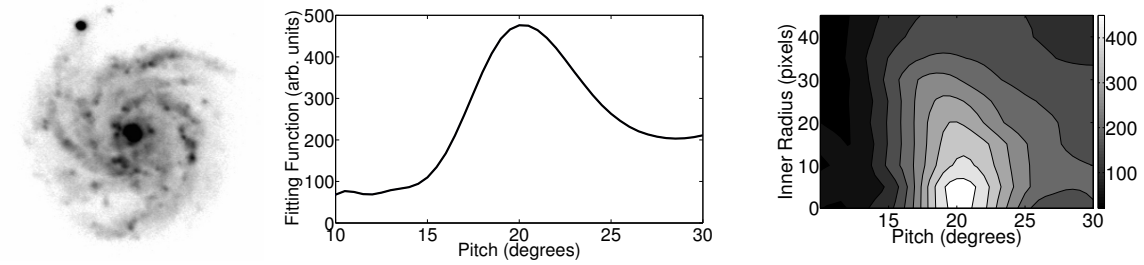

Figure 2.4: Spirality's measurement of the galaxy UGC 463, shown in the **left panel**. **Center:** Fitting function vs. pitch angle for a measurement annulus with inner radius 5 pixels, or 4% of the galaxy's visible radius. The outer radius of the measurement annulus is 115 pixels, or 96% of the galaxy's visible radius. **Right:** Fitting function vs. pitch angle and measurement annulus inner radius. Note that the center panel is a cross section of the right panel. Spirality's measurement gives a best-fit pitch of $19.85° \pm 1.57°$, which is consistent with 2DFFT's measurement of $22.38° \pm 3.21°$

Spirality's measurement gives a best-fit pitch of $19.85° \pm 1.57°$. For comparison,

2DFFT's measurement of the image's 3-arm component is $22.38° \pm 3.21°$. Visual inspection, done by overlaying transparencies marked with spirals of known pitch onto the spiral arms, suggests a pitch of $20° \pm 5°$

With an error bar of only 1.57°, Spirality is particularly confident in this measurement. There are several reasons that combine to make this galaxy easy to measure. First, the absence of foreground stars in the inner part of the image allows Spirality to fit the entire galaxy, not just the 2-arm symmetric component, to the pitch angle templates. Because the spiral arms extend from the central region to the outer edge of the galaxy, Spirality is able to track long segments of the arms. Because the spiral arms are bright, Spirality has no difficulty distinguishing the arms from the space in between. Finally, like many (though certainly not all) spiral galaxies, UGC 463 has arms that are reasonably logarithmic, *i.e.* the pitch does not change much with radius.

2.4.3 Interesting Galaxy: UGC 4256

Occasionally there exists a galaxy with different spirals of different pitch angles. Figure 2.5 shows one such galaxy. UGC 4256 consists of a single, bright, tail-like spiral with a pitch angle of about 45°. The bright spiral overlays two dimmer symmetric spirals with pitch angles of about 30°. This image was found on the NASA/IPAC Extragalactic Database (NED).

When Spirality measures the galaxy as a whole, it fits the single bright spiral to a template of $45.1° \pm 3.8°$. This measurement is consistent with the result from fitting the arm to spirals of known pitch using transparency overlays. 2DFFT, which is known for producing unreliable results in the 1-arm mode, is not able to see this spiral.

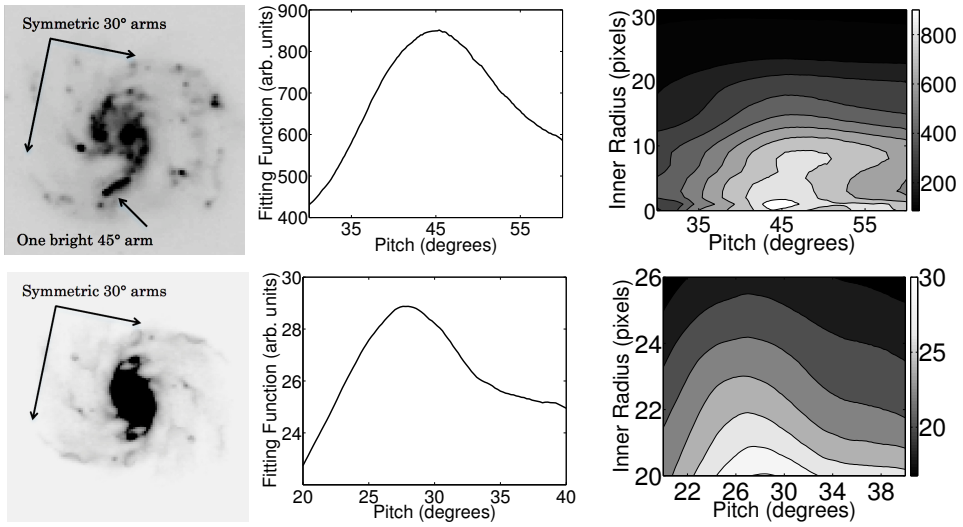

Figure 2.5: Spirality measurements of the galaxy UGC 4256, both the entire galaxy (top row) and the 2-arm component (bottom row). **Top row**, left to right: B-band image of the entire galaxy, fitting function vs. pitch angle at a fixed inner radius, fitting function vs. both pitch angle and inner radius. **Bottom row:** Same as top row, but for the galaxy's 2-arm (180° rotationally symmetric) component, which was computed by SymPart. Note that in each row, the center panel is a cross section of the right panel. For the whole galaxy, Spirality yields a measurement of $45.1° \pm 3.8°$, which is consistent with transparency overlay for the single bright spiral. For the 2-arm component, Spirality yields a measurement of $27.2° \pm 4.1°$, which is consistent with 2DFFT's $29.1° \pm 4.3°$ measurement of the 2-arm mode.

On the other hand, when Spirality measures only the 2-arm symmetric component, the single bright spiral disappears, and the dimmer symmetric spirals come to the fore. Spirality fits the symmetric arms to a template of $27.2° \pm 4.1°$, which is consistent with 2DFFT's 2-mode measurement of $29.1° \pm 4.3°$, and also with the result from transparency overlays.

2.5 Tests on Synthetic Spirals

We conducted numerous tests on synthetically generated spirals in order to determine which regimes Spirality excels and in which regime a different method might be preferable.

These spirals are variants of what we call the "Standard Spiral," a noiseless, logarithmic, synthetically generated spiral with two symmetric arms, pitch angle 20°, radius 100 pixels, arm thickness 4 pixels, and a face-on orientation, with no bar or bulge. We tested 77 synthetic spirals with properties that varied from the Standard Spiral. Additionally, we performed 40 tests on the Standard Spiral with varying input parameters.

2.5.1 Varying Spiral Properties

These synthetic spirals varied from the Standard Spiral in the number of spiral arms, pitch angle, degree of logarithmicity, radius, SNR, inclination angle, bar length, and bulge radius, respectively. The results are summarized in Table 2.1. The table's rows are discussed below.

The number of arms was varied from 1 to 8. Neither the accuracy nor the error bar depended on the number of arms. For all such spirals, the measured pitch was within 0.01° of the true pitch, the total error was less than 0.13°, and the error bar was consistent with the accuracy.

The spiral's true pitch was varied from 5° to 50°, which is the range of pitch angles for most galaxies. The accuracy was slightly reduced and the error bar grew slightly as true pitch increased. For all such spirals, the measured pitch was within 0.4° of the true pitch, the total error was less than 0.8°, and the error bar was consistent with the accuracy.

Spirals with varying deviations from logarithmicity were measured. For each spiral, the true pitch was 20° at the center. The deviation from logarithmicity $\Delta\phi_{True}$ is the difference between the true pitch at the outer rim of the spiral and the true pitch at the center. For example, $\Delta\phi_{True} = 10°$ represents a spiral that varies linearly from 20° at the

Number of spiral arms	1	2	3	4	5	6	8
ϕ	20.01	20.01	20.00	20.01	20.00	20.00	20.01
$\pm$	0.12	0.12	0.10	0.11	0.10	0.10	0.11
True pitch (°)	5	10	15	25	30	40	50
ϕ	5.02	10.03	14.96	24.87	30.23	40.05	49.62
$\pm$	0.12	0.14	0.12	0.48	0.29	0.76	0.72
Deviation from logarithmicity(°)	-19	-15	-10	-5	5	10	15
ϕ	8.41	10.20	13.26	16.25	23.43	26.75	29.99
$\pm$	5.06	3.54	2.04	0.82	0.79	1.86	3.21
Spiral radius (px)	15	20	25	35	50	75	200
ϕ	20.73	20.04	19.66	19.75	20.02	20.03	20.00
$\pm$	1.69	0.82	0.64	0.29	0.12	0.12	0.10
Spiral arm thickness (px)	1	3	6	10	15	20	25
ϕ	19.99	19.97	20.00	20.03	19.72	20.60	19.48
$\pm$	0.12	0.13	0.10	0.45	0.66	1.38	0.79
SNR	16	8	4	2	1	0.5	0.25
ϕ	20.10	20.02	19.96	20.10	20.05	20.23	20.86
$\pm$	0.10	0.18	0.20	0.20	0.64	0.50	0.73
Inclination(°)	5	10	15	20	25	30	35
ϕ	20.17	20.30	20.46	20.74	20.68	20.63	21.59
$\pm$	0.34	0.56	1.26	2.27	3.54	5.15	7.61
Bar half-length (px)	10	20	30	40	50	60	70
ϕ_{center}	20.11	20.15	20.18	20.21	20.27	33.19	40.18
$\pm$	0.18	0.18	0.18	0.18	0.21	14.32	15.70
ϕ_{bar}	20.02	20.02	20.03	20.00	20.11	20.02	20.13
$\pm$	0.14	0.12	0.13	0.10	0.15	0.14	0.19
Bulge radius (px)	10	20	30	40	50	60	70
ϕ_{center}	20.06	20.05	20.04	20.04	20.09	20.10	20.10
$\pm$	0.11	0.11	0.11	0.11	0.10	0.10	0.10
ϕ_{bulge}	20.00	20.02	20.01	20.00	20.11	20.02	20.13
$\pm$	0.10	0.11	0.11	0.10	0.15	0.13	0.20

Table 2.1: Test results (pitch ϕ and error $\pm$) for variations of the standard synthetic spiral, defined as having two logarithmic arms with pitch 20°, radius 100 px, thickness 4 px, no noise, face-on orientation, and no bar or bulge. Each triplet of rows shows a variation on one of the spiral's properties. For each triplet, the top row shows the value of the quantity being varied, the middle row shows the measured pitch, and the bottom row shows the measurement uncertainty. For Spirality's input parameters, we used the so-called optimal inputs described in Table 2.2. **Deviation from logarithmicity:** Linear change in pitch angle from the center to the edge. The pitch remains 20° at the center. **SNR:** Signal-to-noise ratio, where Gaussian noise is added to the image. **Inclination:** Projection of the logarithmic spiral onto an inclined plane before measurement. **Bulge or bar radius:** Radius of circular bulge or length of elliptical bar added to the galactic center. For measurements labeled ϕ_{center}, the measurement is taken over the entire spiral, including the bulge or bar. For measurements labeled ϕ_{bulge} or ϕ_{bar} the measurement excludes bulge or bar.

center to 30° at the outer rim. Because Spirality's templates are logarithmic, we would expect the code to output large error bars for nonlogarithmic spirals. Indeed, greater values of $\Delta\phi_{True}$ (that is, less logarithmic spirals) yielded measurements with larger error bars. However, the measured pitch was usually consistent with the spiral's mean true pitch as a function of radius. For 5 of the 7 spirals, the measured pitch was less than 1 error bar away from the mean true pitch. For each of the remaining 2 spirals, the measured pitch was less than 1.6 times the error bar away from the mean true pitch.

The spiral radius was varied from 15 pixels to 200 pixels. The error bar shrank, and the accuracy improved, as the spiral grew in radius. For all such spirals, the measured pitch was within 0.7° of the true pitch, the total error was less than 1.7°, and the measured pitch was within 1.1 times the error bar away from the true pitch.

The spiral arm thickness was varied from 1 pixel to 25 pixels. The error bar grew, and the accuracy suffered, as the thickness increased. For all such spirals, the measured pitch was within 0.6° of the true pitch, the total error was less than 1.4°, and the error bar was consistent with the accuracy.

Varying amounts of Gaussian noise were added to the spiral image. Here, SNR is defined as the mean pixel value of the spiral arm divided by the standard deviation of the Gaussian noise distribution. The mean pixel value of the empty space between the arms was zero. Noise was added to both the spiral arms and the empty space. The SNR varied from 16 down to 0.25. The error bar increased, and the accuracy suffered, as the SNR decreased. For all such spirals, the measured pitch was within 0.9° of the true pitch, the total error was less than 0.8°, and the measured pitch was less than 1.2 times the error bar away from the

true pitch.

For a galaxy, the inclination angle would be estimated or measured, and the galaxy deprojected to face-on, before the pitch is measured. However, inclination angles can be challenging to find. Therefore it is prudent to know how much leeway a pitch angle measurement tool allows for mismeasuring the inclination angle. For this test, the synthetic spiral was compressed along the y-axis in order to simulate viewing the spiral at inclination angles varying from 5° (*i.e.*, nearly face-on) to 35°. The result is that the error bar grew substantially, but the accuracy only suffered slightly, as the inclination increased. For all such spirals, the measured pitch was within 1.6° of the true pitch, and the error bar was consistent with the accuracy. We find that Spirality states the correct pitch angle even if a galaxy's inclination is incorrectly deprojected. However, the measurement yields unreasonable error bars if the galaxy retains an inclination of more than 20° after deprojection.

The central section of the spiral image was replaced by an elliptical bar with an axis ratio of approximately 1.7. The bar's half-length, or semi-major axis, varied up to 70 pixels. When the measurement annulus included the elliptical bar, the error bar increased substantially and the accuracy suffered substantially if the bar's half-length was more than 50 pixels (*i.e.*, if the elliptical bar consumed more than half the radius of the spiral). For spirals with bar half-lengths of 50 pixels or less, the total error was less than 0.3° and the measured pitch was less than 1.3 times the error bar away from the true pitch. On the other hand, when the measurement annulus was placed outside the elliptical bar (as would be the case in a galaxy measurement), neither the error bar nor the accuracy were substantially affected by the elliptical bar. For all such measurements, the total error was less than 0.2°

and the accuracy was consistent with the error bar.

The central section of the spiral image was replaced by a circular bulge, the radius of which varied up to 70 pixels. When the measurement annulus included the bulge, the total error was less than 0.2° and the accuracy was consistent with the error bar. When the measurement annulus was placed outside the bulge, the total error was less than 0.3° and the accuracy was consistent with the error bar.

2.5.2 Varying Inputs

The Standard Spiral defined in the opening paragraph of Section 2.5 was measured with varying inputs to the Spirality code. The results are summarized in Table 2.2.

A galaxy's center can be estimated, though the estimate contains some error. It is therefore helpful to know how much leeway a pitch angle measurement tool allows for the mismeasurement of a galaxy's center. For this test, the center offset is defined as the difference, in pixels, between the center of the spiral and the center of the measurement annulus. Each pixel represents 1% of the spiral's radius. The center offset was varied from 0 to 10 pixels. For all such measurements, the error bar was consistent with the accuracy. The error bar was highly sensitive to the center offset, though the accuracy was only mildly affected. For example, when the center offset was less than or equal to 8 pixels, the measured pitch was within 0.12° of the true pitch. However, with a center offset of 8 pixels, the error bar had already grown to more than 10°. For galaxies in which the center is difficult to obtain, we recommend varying the center coordinates of the measurement annulus until the error bar is minimized.

Spirality's error bars are determined using the method of Davis et al. (2012), in which

Center offset (px)	0	1	2	3	4	6	8	10
ϕ	20.01	19.94	20.01	19.88	19.95	20.12	19.96	22.03
$\pm$	0.12	0.12	0.31	2.18	4.04	6.95	10.15	13.41
Inner radius spacing (px)	2	3	4	5	10	15	20	25
ϕ	20.02	20.02	20.02	20.02	20.01	20.02	20.03	20.00
$\pm$	0.11	0.12	0.12	0.12	0.12	0.12	0.13	0.10
Number of spiral axes	1	5	10	50	100	500	1000	4000
ϕ	21.00	20.70	20.70	19.00	19.20	19.81	19.82	19.83
$\pm$	0.10	0.10	0.10	0.10	0.21	0.24	0.16	0.16
Pitch angle spacing (°)	0.1	0.2	0.3	0.5	0.75	1	3	5
ϕ	20.00	20.00	19.86	20.00	19.75	20.00	19.00	20.00
$\pm$	0.10	0.20	0.44	0.50	0.75	1.00	3.00	5.00
Axis point spacing (px)	0.25	0.5	0.75	1	1.25	1.5	1.75	2
ϕ	19.91	19.91	19.93	19.87	19.97	19.84	19.80	19.96
$\pm$	0.12	0.25	0.15	0.18	0.27	0.20	0.10	0.18

Table 2.2: Test results (pitch ϕ and error $\pm$) after varying the optimal inputs on the so-called standard synthetic spiral described in Table 2.1. The optimal inputs, as defined here, are that the measurement annuli are centered with the spiral, their inner radii are spaced 10 pixels apart, the outer radius of all measurement annuli is 99 pixels (in agreement with the outer radius of the spiral), 650 spiral axes are computed for each pitch angle template, the pitch angle templates are computed at intervals of 0.1°, and each spiral axis on each template consists of points spaced 0.1 pixels apart. Each triplet of rows shows a variation on one of Spirality's input parameters. For each triplet, the top row shows the value of the quantity being varied, the middle row shows the measured pitch, and the bottom row shows the measurement error. **Center offset:** The number of pixels between the spiral's true center and the center of the measurement annuli. **Inner radius spacing:** The number of pixels between inner radii of successive measurement annuli. **Number of spiral axes:** Number of spiral coordinate axes computed for each pitch angle template. **Pitch angle spacing:** Number of degrees between successive pitch angle templates. **Axis point spacing:** Number of pixels between successive computation points on a given spiral axis.

the pitch angle is measured on several measurement annuli. Each annulus has the same outer radius but a different inner radius. The spacing, in pixels, between successive inner radii is input. The smaller the inner radius spacing, the more annuli are measured. For this test, the inner radius spacing was varied from 2 to 25 pixels. For all such measurements, the error bar was less than 0.14°, and was consistent with the accuracy.

We recommend a two-step measurement process for galaxies. In the first measurement, which we call the "coarse" measurement, the inner radius begins just outside the bar or bulge, and is varied outward with a sufficiently small inner radius spacing to allow about 10 different inner radii between the bulge/bar and the outer radius. Once a region of inner radii of roughly constant pitch is identified, a second measurement (the "fine" measurement) is conducted. The fine measurement is "zoomed in", both on the stable radius segment and on the resulting pitch angle. In other words, the second measurement includes 10 inner radii that span only the stable region rather than the galaxy as a whole, and only look at pitch angle templates that are near the true pitch.

The number of spiral axes on the templates was varied from 1 to 4000. When the number of spiral axes was at least 500, or 5 times the spiral's radius in pixels, the error bar was less than 0.25°, and the measured pitch was within 1.2 times the error bar away from the true pitch. For galaxy measurements, we recommend at least $4\pi R$ spiral axes, where R is the galaxy's radius in pixels. That way, each pixel on the outer rim of the measurement annuli gets counted, on average, twice. If the image is sufficiently large that computation time becomes an issue, the number of spiral axes can be reduced to $2\pi R$, thus counting each outer pixel, on average, once.

The spacing, in degrees, between the pitch angles of successive templates is input. The pitch spacing is the so-called "quantized error" described by Davis et al. (2012). As such, it is the minimum possible error bar. For this test, the pitch spacing was varied from 0.1° to 5°. For all such measurements, the measured pitch was within 0.25° of the true pitch, and the error bar was consistent with the accuracy. However, since the pitch spacing is also the quantized error, the error bar grew with the pitch spacing.

For the two-step galaxy measurement described above, we recommend a pitch spacing of 1° for the course measurement and 0.2° for the fine measurement. The fine measurement should be zoomed into a pitch angle domain on which the fitting function's peak is a global max. If the quantized error contributes significantly to the overall error, the code will generate a warning. The solution is to reduce the pitch spacing.

The spacing, in pixels, between successive computation points on a given spiral axis is input. For this test, the axis point spacing was varied from 0.25 pixels to 2 pixels. When the axis point spacing was 1.5 pixels or less, the measured pitch was within 0.16° of the true pitch and the error bar was consistent with the accuracy. For galaxy measurements, we recommend an axis point spacing of at most 0.25 pixels. If the image is sufficiently large that computation time becomes an issue, the axis point spacing may be increased to 0.5 pixels.

2.6 Tests on Galaxy Samples

We tested Spirality on three samples of galaxies: the nearby sample defined by the DMS PPak (Martinsson et al., 2013), the nearby sample defined by Pour Imani et al. (in prep), and a distant sample of visually identified spirals in GOODS North and South (Gi-

avalisco et al., 2004).

Tests were conducted by comparing Spirality pitch angle measurement results with those produced by 2DFFT, and also by overlaying the galaxies with spirals of known pitch via transparencies. In some cases, where high-resolution images and low-resolution images were available for the same galaxy, Spirality was tested by comparing its measurement of high resolution image to its measurement of the low-resolution image.

For these tests, we define the "disagreement factor" as the difference between the two codes' results divided by the sum of the error bars. If the disagreement factor is less than one, Spirality's measurement is consistent with 2DFFT's measurement. If the disagreement factor is equal to one, Spirality's error bar barely touches 2DFFT's error bar. If the disagreement factor is greater than one, the error bars to not overlap.

2.6.1 Nearby Galaxies: DMS PPak

The sample defined by DMS PPak (Martinsson et al., 2013) contains 30 nearby galaxies. Spirality's pitch angle measurements are consistent with 2DFFT's pitch angle measurements for 26 of those galaxies, as shown in Table 2.3.

For this sample of nearby galaxies, 2DFFT is more confident about its measurements than Spirality. Spirality's error bars for the this sample have a mean of 3.6° and a standard deviation of 2.4°. 2DFFT's error bars have a mean of 3.0° and a standard deviation of 1.4°.

The four galaxies for which Spirality disagrees with 2DFFT are discussed in the subsections below.

Galaxy Name	Type	Band	Image Source	Spirality Pitch (°)	2DFFT Pitch (°)
UGC 448	SABc	r	1	-15.1 ± 4.9	-18.1 ± 1.7
UGC 463	SABc	B	4	19.9 ± 1.6	22.4 ± 3.2
UGC 1081	SBc	r	1	24.6 ± 2.0	24.3 ± 3.1
UGC 1087	Sc	r	1	9.7 ± 5.1	10.6 ± 2.2
UGC 1529	Sc	B	4	-28.3 ± 3.3	-26.1 ± 4.4
UGC 1635	Sbc	r	1	9.3 ± 1.5	11.8 ± 0.8
UGC 1862	SABcd[1]	r	1	27.4 ± 8.1	23.9 ± 3.5
UGC 1908	SBc[2]	B	4	22.4 ± 1.1	20.6 ± 3.5
UGC 3091	SABd	i	1	-14.6 ± 5.9	-29.5 ± 4.0
UGC 3140	Sc	r	1	-19.7 ± 1.8	-16.2 ± 4.8
UGC 3701	Scd	r	1	-14.8 ± 4.7	-15.4 ± 4.8
UGC 3997	Im	g	2	-16.2 ± 2.5	-10.5 ± 2.6
UGC 4036	SABbc	B	4	-16.9 ± 4.1	-15.0 ± 1.1
UGC 4107	Sc	g	2	-24.3 ± 3.1	-20.4 ± 2.1
UGC 4256	SABc	g	2	45.1 ± 3.8	29.1 ± 4.3
UGC 4368	Scd	g	2	29.7 ± 6.8	23.7 ± 2.1
UGC 4380	Scd	g	2	-15.4 ± 4.3	-23.3 ± 4.6
UGC 4458	Sa	g	2	-9.7 ± 4.0	-13.6 ± 3.0
UGC 4555	SABbc	g	2	12.6 ± 0.5	12.1 ± 1.0
UGC 4622	Scd	g	2	-15.1 ± 3.3	-21.8 ± 4.9
UGC 6903	SBcd	g	2	-14.8 ± 2.1	-15.8 ± 2.2
UGC 6918	SABb[3]	F606W	3	-15.2 ± 1.2	-17.0 ± 2.3
UGC 7244	SBcd	g	2	25.7 ± 11.6	32.1 ± 4.3
UGC 7917	SBbc	g	2	-14.2 ± 4.9	-15.5 ± 1.4
UGC 8196	Sb	g	2	-7.3 ± 1.6	-8.2 ± 0.5
UGC 9177	Scd	g	2	-12.7 ± 2.9	-14.4 ± 1.9
UGC 9837	SABc	g	2	28.6 ± 4.6	25.7 ± 2.8
UGC 9965	Sc	g	2	-12.7 ± 2.2	-13.3 ± 2.0
UGC 11318	SBbc	B	4	-34.7 ± 2.9	-29.7 ± 4.4
UGC 12391	SABc	r	1	-11.3 ± 0.8	-13.2 ± 5.0

Table 2.3: Spirality vs. 2DFFT pitch angle measurements for nearby galaxies. **Columns: (1)** Galaxy name. **(2)** Hubble morphological type from either the UGC (Nilson, 1973) or RC3 (de Vaucouleurs et al., 1991) catalogs. Notes on morphologies: 1 = peculiar, 2 = starburst, and 3 = AGN. **(3)** Filter waveband/wavelength used for pitch angle calculation. **(4)** Telescope/literature source of imaging: 1 = WIYN 3.5 m pODI; 2 = SDSS; 3 = HST; 4 = Kitt Peak 2.1 m. **(5)** Pitch angle as measured by Spirality. **(6)** Pitch angle as measured by 2DFFT, from Davis et al. (2015)

UGC 1635 The disagreement factor for this galaxy was 1.09. Although the error bars did not quite overlap, the Spirality's measurement was very nearly consistent with 2DFFT's.

UGC 3091 With a disagreement factor of 1.5, Spirality's result disagrees significantly with 2DFFT's result. The respective error bars of 5.9° and 4.9° show that neither code is particularly confident in its measurement. This galaxy has a low surface brightness, and its spiral structure is difficult to make out by visual inspection. Such galaxies pose a challenge to any pitch angle measurement code.

UGC 3997 This is a particularly interesting case. When one of our researchers measured this galaxy using Spirality, and another using 2DFFT, without communicating with one another, the researchers reached a disagreement factor of 1.12, as indicated in Table 2.3. Afterward, when the researchers compared results, they found that 2DFFT had been instructed to measure the spirals in the outer disk, while Spirality had been instructed to measure the spirals in the inner disk. When Spirality's measurement annulus was adjusted to match 2DFFT's, Spirality produced a result of -12.4° ± 0.9°, which is consistent with 2DFFT's result.

This case serves as a cautionary tale for any pitch angle measurement algorithm that assumes a logarithmic spiral, *i.e.* that declares a best-fit pitch. Such a declaration is useful because global spiral arms are often well-described as logarithmic, although future versions of Spirality will incorporate pitch angle templates that vary with radius. When assuming a constant pitch and thus reducing the spiral structure to a single quantity, a measurement annulus must be declared. Whether the annulus is determined by inspection or by analysis, the resulting best-fit pitch may well depend on the annulus. For galaxies in which the structure is too complex to be described by a single quantity, researchers may choose to analyze individual spiral arms or spiral arm segments. Such analysis can be done using

methods such as SpArcFiRe, which was introduced in Davis & Hayes (2014).

UGC 4256 This galaxy is discussed in Section 2.4.3 and shown in Figure 2.5. The two methods' disagreement on the pitch angle of this galaxy stems from 2DFFT's assumption of 2-arm symmetry. The disagreement is resolved when Spirality is directed to measure only the 2-arm component.

2.6.1.1 Measurement Quality of Low-Resolution Images

We have found that measurement quality depends strongly on the radius, in pixels, of the galaxy image.

For many of the galaxies listed in Table 2.3, we had access to both high-resolution imaging and low-resolution imaging. For each galaxy where such imaging was available, we used Spirality to measure the pitch angle of the low-resolution image, and also of and the high-resolution image, and compared the results. We declared each result a "confirmed" measurement if the result was consistent with Spirality's measurement of the same galaxy at a different resolution, or else if the result was consistent with 2DFFT's measurement of the same image.

For the 30 galaxies in Table 2.3, a total of 44 images were analyzed. 23 of those images had galactic radii of 30 pixels or less, while the remaining images had galactic radii of 35 pixels or more.

For galaxies of radius $\geq$35 pixels, 100% of the pitch angle measurements were confirmed either by higher resolution imaging or by an independent method of measurement. For galaxies of radius $\leq$ 30 pixels, only 43% of the measurements were confirmed.

This result underscores the importance of having adequate image resolution if a pitch angle measurement is to be trusted.

2.6.2 More Nearby Galaxies: Pitch Angle vs. Wavelength

Pour-Imani et al. (2016) measured 40 nearby spirals in three wavelength bands: B (new stars), 8.0 μm (starforming dust) and 3.6 μm (old stars). All measurements were taken using both Spirality and 2DFFT, shown in Figure 2.6.

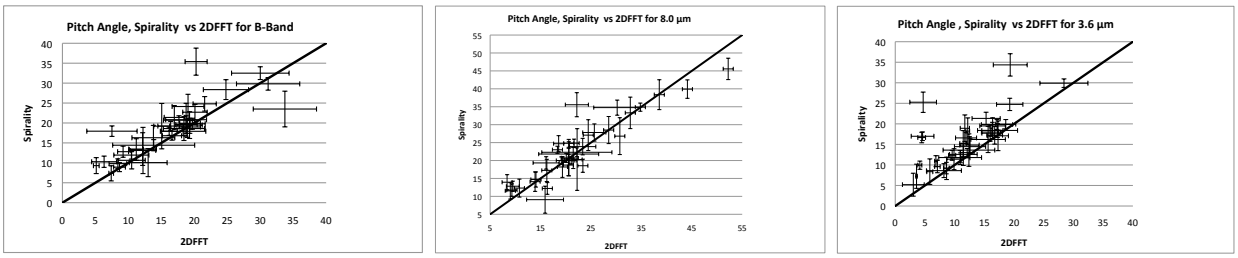

Figure 2.6: Spirality vs. 2DFFT measurements of 40 nearby spiral galaxies from Spitzer. Measurements were taken in three wavelength bands: 445nm (B-Band, **left**), 3.6 μm (**center**) and 8.0μm (**right**) for unbarred, intermediate and barred galaxies. In each panel, the diagonal line is $y = x$.

In the B-band and 3.6 μm band, the pitch angle results are mostly consistent. However, in those galaxies where the results are not consistent, Spirality shows a systematic tendency toward looser pitch angles. The average difference between the two codes' results is 4.0° for 3.6 μm and 3.1° for B-band.

In the 8.0 μm images the average difference is 3.6° and there is no systematic bias.

We infer that the 8.0 μm band, which tracks dust, provides smoother spiral arms and is thus easier for both codes to measure. The other two bands, which track young stars (B-Band) and old stars (3.6 μm), provide clumpier spirals, which tend to be read as looser by Spirality than by 2DFFT.

The total average difference is 3.5° for all 40 galaxies, but is reduced to 1.8° when we only consider the 17 unbarred spirals.

2.6.3 High Redshift, Low Resolution Galaxies

Measuring the pitch angles of distant galaxies represents a unique challenge. Many spirals in the GOODS sample, for example, have small angular radii and are quite noisy. Moreover, there is debate as to whether such galaxies even exhibit *bona fide* spiral structure. Guo et al. (2015) argue that many galaxies at $z \geq 0.5$ exhibit large clumps of stars rather than logarithmic spirals. It would be no surprise if Spirality and 2DFFT, which both assume logarithmic spirals, would have difficulty coming to agreement on the pitch angle of a galaxy which may in fact be nowhere near logarithmic.

Indeed, the low resolution of distant GOODS galaxies was a key motivation for developing Spirality. We wanted to find an independent pitch angle measurement technique that would serve as a comparison to 2DFFT's results. If the two methods agree on a galaxy's pitch angle, then we gain confidence that the galaxy approximates a logarithmic spiral.

Figure 2.7 shows a particularly difficult example. In addition to being distant ($z = 1.2$) and having a small pixel radius (30 px), the galaxy also has a visual companion that is not shown in the figure. The visual companion evokes the suspicion that the galaxy may not be logarithmic at all. It is not surprising, then, that Spirality and 2DFFT differ wildly on the results of this pitch angle. Their respective measurements are $-30.2° \pm 4.0°$ and $+37.9° \pm 6.7°$, which amounts to a disagreement of $D = 6.3$. Such a galaxy would be deemed to have an unreliable pitch angle for the purposes of scientific analysis.

Figure 2.8 shows the pitch angle measurements of 203 visually selected spirals from

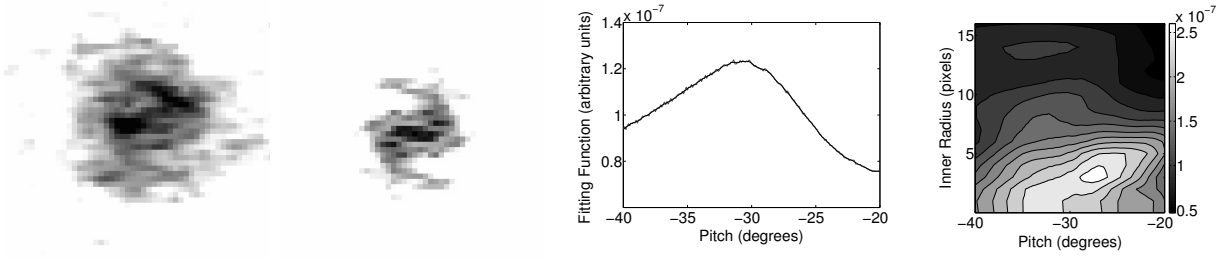

Figure 2.7: Spirality's measurement of a low-resolution galaxy from the GOODS sample. The **left panel** shows the entire galaxy, while the **center panel** shows the 2-arm symmetric mode, as computed by Spirality. The **right panel** shows the pitch angle measurement of the 2-arm mode at a fixed inner radius, and the right panel shows the measurement with variable inner radius. No reasonable measurement could be obtained for the galaxy as a whole; the right two panels describe only the 2-arm mode. Spirality's measurement of the 2-arm mode is $-30.2^\circ \pm 4.0^\circ$, as compared to 2DFFT's measurement of $+37.9^\circ \pm 6.7^\circ$. Such a wide disagreement would cause us to expel this galaxy from any sample that is used for scientific analysis.

the GOODS sample using both Spirality and 2DFFT. It should be noted that galaxies with high disagreement factors are included here. The two codes agree on chirality (the sign of the measurement) for 94% of galaxies. The measurements agree within their error bars on 64% of the galaxies. When the codes disagree, Spirality on average sees a tighter (closer to zero) pitch angle than 2DFFT.

In order to take the error bars into account when computing the regression, we expressed each data point as a bivariate Gaussian cloud of 100 randomly generated points. Each cloud is centered at the point (Φ_{2D}, Φ_{Sp}), where Φ_{2D} is the 2DFFT measurement and Φ_{Sp} is the Spirality measurement. The horizontal distribution of points for each cloud is normal, with the standard deviation being the error in the 2DFFT measurement. Likewise, the vertical distribution of points for each cloud is also normal, with the standard deviation being the error in the Spirality measurement.

The 20,300 total cloud points (100 for each of 203 galaxies) were regressed using an

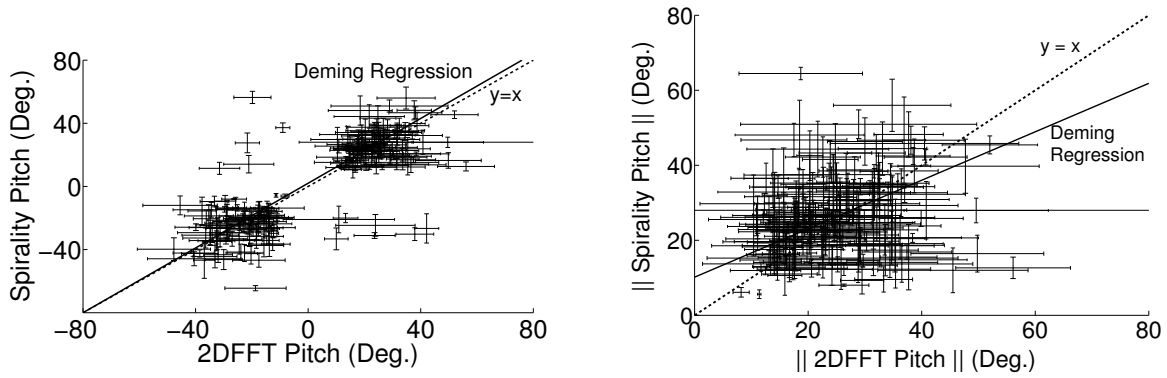

Figure 2.8: Spirality measurements vs. 2DFFT measurements of visually selected spirals in the GOODS North and South samples. For each plot, the solid line represents the orthogonal least squares (Deming) regression, while the dashed line represents $y = x$. **Left panel:** all 203 visually selected spirals. **Right panel**, absolute values for the 191 galaxies for which Spirality and 2DFFT agree on chirality.

orthogonal (Deming) least squares fitting, as described in Kermack & Haldane (1950) and revisited in York (1966). With this method, the error in the slope decreases as $\frac{1}{\sqrt{N}}$, where N is the number of data points. Since our Gaussian clouds artificially increased N by a factor of 100, we multiplied the resulting slope error by 10 to compensate. It should be noted that the error bars, not the Gaussian clouds, are shown in Figure 2.8.

The left panel of Figure 2.8 shows all 203 galaxies, with chirality information (positive or negative) left in tact. The slope of the Deming regression, 1.06 ± 0.66, is highly consistent with $y = x$, which illustrates the degree to which the two codes agree on chirality. The intercept, $(-1 \pm 20)^\circ$, is consistent with zero, though the large error bar illustrates the high amount of random disagreement between the two codes for this sample of low-resolution galaxies.

The right panel of Figure 2.8 shows only those 191 galaxies for which Spirality agrees with 2DFFT about the chirality. This plot shows the absolute values of those measurements.

The slope of the Deming regression, 0.63±0.31, is not consistent with $y = x$. This indicates that for poorly resolved galaxies such as these, Spirality tends to see a tighter (closer to zero) pitch than 2DFFT. The intercept is $(10 \pm 24)°$.

For this noisy sample of images, Spirality is more confident about its measurements than 2DFFT. Spirality's error bars for the GOODS sample have a mean of 4.8° and a standard deviation of 2.6°. 2DFFT's error bars have a mean of 7.1° and a standard deviation of 4.4°.

2.6.3.1 Testing the Error Bars

One would expect a random error distribution to be distributed more or less normally. The respective error bar distributions of Spirality and 2DFFT for the GOODS sample measurement are shown in Figure 2.9.

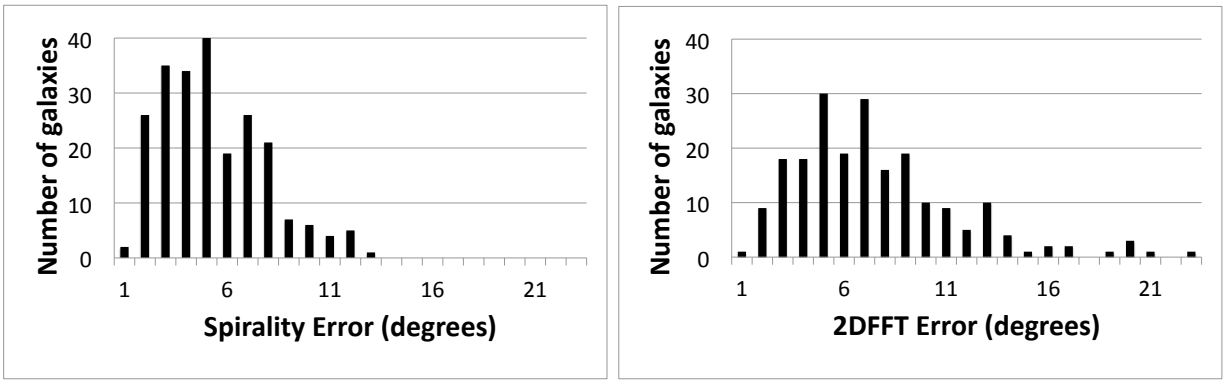

Figure 2.9: Error bar distributions for GOODS North and South pitch angle measurements of 203 galaxies by Spirality (**left**) and 2DFFT (**right**). In the right panel, a single outlier data point corresponding to a 2DFFT error of 45° is omitted.

Based on the Cramèr-von Mises test, the null hypothesis that Spirality's errors are distributed normally cannot be rejected at the 5% level. The test yields a P-value of 0.10. On the other hand, based on the same test, the null hypothesis that 2DFFT's errors are distributed normally is rejected. The test yields a P-value of 0.0015.

By measuring the same galaxies using both 2DFFT and Spirality, we can begin to understand the regimes in which the codes are likely to agree within their error bars. When the codes agree, we gain confidence in the measurements.

Recall from Subsection 2.6.1 that the disagreement factor D is the difference between the Spirality measurement and the 2DFFT measurement, divided by the sum of the error bars. Therefore, if $D \leq 1$ for a galaxy, the codes agree on the galaxy's pitch angle within the error bars. While the two codes agree to within a disagreement factor of 1.1 for 90% of the nearby galaxies in the sample defined by the DMS PPak, they only agree 64% of the time in low-resolution images of GOODS North and South.

In order to get an idea of which galaxy properties (or combinations of properties) produce easily measurable pitch angles, we produced a series of 3-D histograms that showed the number of galaxies vs. disagreement factor and one other property (or a combination of two other properties). The histograms are shown in Figure 2.10.

The independent properties under analysis in Figure 2.10 are galaxy radius in pixels, i-band magnitude, and redshift. These properties are vastly different in numerical scale, so in order to combine them, we scaled each of them as a so-called quality factor from approximately zero (low quality) and approximately unity (high quality). That way, the properties can be combined as a geometric mean, and the result will also be a quality factor between zero and unity. We chose the geometric mean instead of the simple product because the simple product would combine two equal values to produce a smaller value, while the geometric mean combines two equal values to produce the same value.

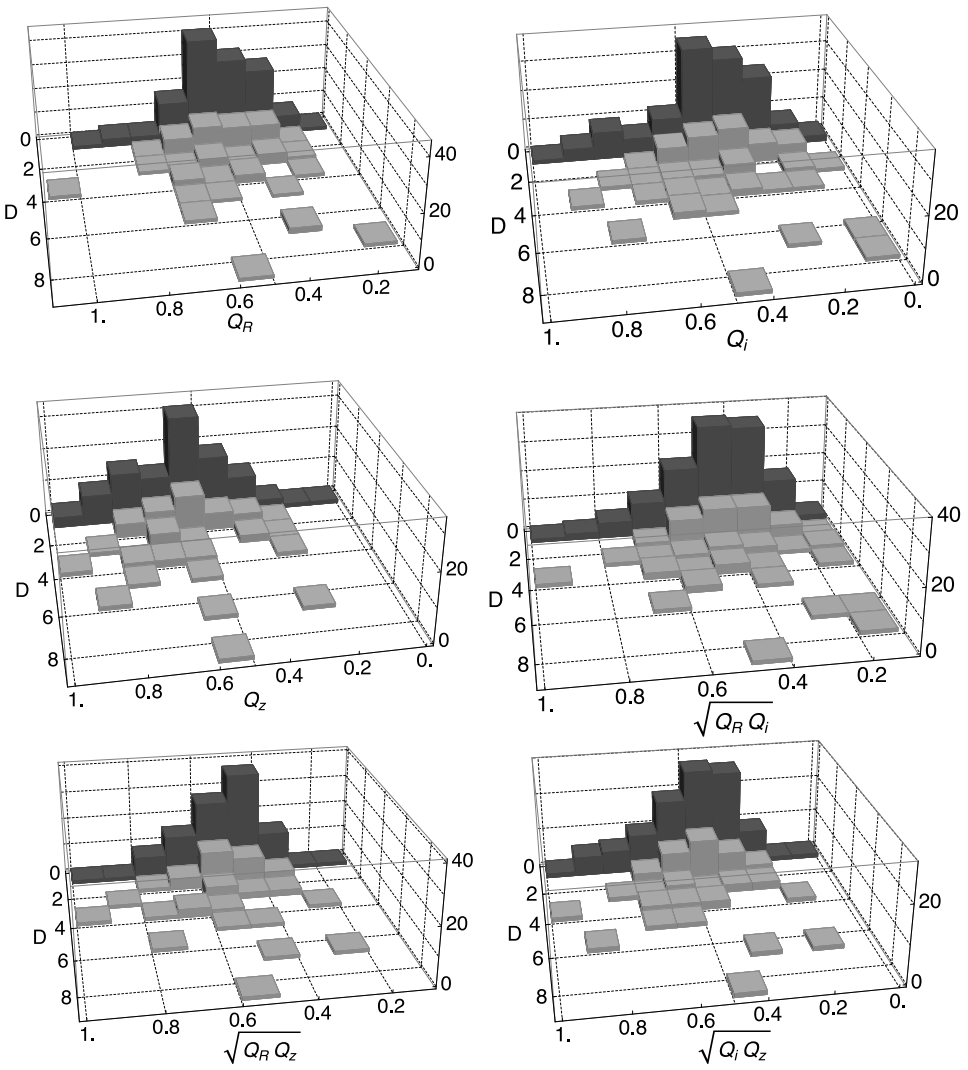

Figure 2.10: Histograms showing the disagreement factor (difference in the measurements divided by the sum the of errors) between Spirality and 2DFFT for galaxies in GOODS North and South. The disagreement factor D indicates the trustworthiness of the codes' error bars. In each panel, dark gray histogram bars show galaxies for which $D < 1$, **i.e.**, for which Spirality's pitch angle measurement is consistent with 2DFFT's measurement within the error bars. The light gray histogram bars show galaxies for which the codes disagree. The second independent variable is different for each panel. **Top left:** Radius quality, which is the galaxy's angular radius in pixels, scaled logarithmically such that its value for the largest galaxy is approximately unity. **Top right:** Brightness quality, which is the i-band magnitude, scaled linearly such that its value for the brightest galaxy is approximately unity and for the dimmest galaxy is approximately zero. **Middle left:** Distance quality, which the redshift, scaled linearly such that its value for the nearest galaxy approaches unity and for the most distant galaxy approaches zero. **Middle right:** Geometric mean of radius quality and brightness quality. **Bottom left:** Geometric mean of radius quality and distance quality. **Bottom right:** Geometric mean of brightness quality and distance quality.

The respective quality factors for radius, brightness, and redshift are:

$$Q_R = \frac{1}{3.5} ln \left(\frac{R}{270} \right) \tag{2.5}$$

$$Q_i = \frac{25 - i}{8} \tag{2.6}$$

and

$$Q_z = \frac{1.7 - z}{1.7} \tag{2.7}$$

where R is the galaxy radius in pixels, i is the i-band magnitude, and z is the redshift.

Figure 2.10 shows that agreement between between Spirality and 2DFFT correlates to some, but not all, combinations of quality factors. First, the bin with the lowest brightness quality Q_i shows more disagreement than agreement. This implies the intuitive result that a dim (or, equivalently, noisy) galaxy is difficult to measure. Second, when the combination $\sqrt{Q_R Q_i}$ of brightness quality and radius quality is low, disagreement is likely. We therefore infer that the outer regions of the disk, being generally dimmer than the inner regions, are more likely to be lost in the noise. Image noise therefore decreases the effective pixel radius on which the galaxy can be measured. Not surprisingly, disagreement shows a correlation with outer radius: the larger the galaxy, the more likely the codes are to agree. This is in line with observations of high-quality images (Section 2.6.1.1).

It should be noted that these quality factors are sample-dependent. No conclusion should be made about the codes' ability to agree on specific magnitudes, because the SNR of a galaxy image depends on the optics of the telescope and the exposure time in addition to the magnitude. In this sample, all galaxies are captured with the same optics (HST ACS),

and all galaxies have exposure times of about 5 days.

The surprising result is that the disagreement factor does not correlate strongly with redshift. The difficulty the codes had in measuring galaxies in the GOODS field is therefore due more to image quality than to redshift. This is consistent with spiral structure being fully formed in many galaxies by z=1.2, the distance inside which 95% of our sample lies.

2.7 Advantages of Spirality vs. 2DFFT

The primary advantage of Spirality is that it doesn't assume a specific number of arms. 2DFFT, on the other hand, yields different results for the 2-arm mode, the 3-arm mode, etc., and the user must choose the most meaningful mode. Sometimes, *e.g.* for a grand design 2-arm spiral, the choice of modes is obvious, and 2DFFT provides quantifiable methods to confirm the user's decision. Other times, *e.g.* for a flocculent galaxy, no single mode may dominate. The act of choosing a mode requires the user to discard the other modes, which may include nontrivial information. While Spirality has the option to focus on a single mode, by default it analyzes the whole of the galaxy, without throwing away any information.

Additionally, the output of Spirality's component code SpiralArmCount provides a clear way to count the spiral arms without assuming rotational symmetry, and also provides a visual representation of arm-interarm contrast.

Future versions of Spirality will introduce templates that vary the pitch angle as a function of radius.

The advantage of 2DFFT's mode decomposition, on the other hand, is that foreground

stars generally have no conjugate counterparts, and therefore get stored in the 1-arm mode. Therefore, except in the unusual case of a 1-arm galaxy, 2DFFT is less sensitive to foreground stars than Spirality. In fact, the presence of even a single foreground star can introduce a monotonic background function in Spirality's fitting function, causing the best-fit pitch to occur at a local maximum rather than a global maximum.

2.8 Future Work

We are working to desensitize Spirality to foreground stars by changing the fitting function from the variance of means to the variance of medians. As a statistical indicator, the median is much less sensitive to outliers than the mean. In context of a galaxy image, a foreground star is an outlier in terms of pixel value. Therefore, we believe that the variance of medians will be less sensitive to foreground stars than the variance of means. Initial tests have confirmed this hypothesis.

Additionally, we are working to generalize Spirality so that it does not assume a logarithmic spiral. Once the best-fit pitch is determined, the corresponding logarithmic spiral template will be used as a starting point, and templates computed in which the pitch angle varies with the radial coordinate. The result will not be a best-fit pitch, but rather a best-fit pitch as a function of radius.

3 Pitch Angle Analysis of Galaxies with Spiral Structure Between Redshifts 2.0 and 2.4

We present pitch angle analysis of two spiral galaxies beyond redshift 2, one of which appears to be a clear one-arm logarithmic spiral and the other a clumpy spiral. For each galaxy, the analysis was made using both a variable inner radius two dimensional Fast Fourier Transform (2DFFT) and the Spirality template fitting software. The redshift 2.3219 galaxy GS21 (J2000 RA 53.14863°, Dec -27.95469°) has a pitch of approximately -10.6° ± 1.6°. The redshift 2.011 galaxy GZ5001 (J2000 RA 189.14811°, Dec 62.24002°) has a pitch of approximately 16.2° ± 2.6°. The relatively small error bars suggest that the galaxies may approximate logarithmic spirals, which is a common property among low-redshift galaxies.

The first galaxy (hereafter, GS21) is from GOODS South, section 21. The second galaxy (hereafter, GZ5001) was identified in Galaxy Zoo: Hubble (Willett et al., 2017). Both are shown in Figure 3.1.

GS21 was imaged through the F814W filter by the Advanced Camera for Surveys (ACS) aboard Hubble Space Telescope (HST). VLT/VIMOS (Balestra et al., 2010) measured a spectroscopic redshift of 2.3219, and applied a confidence flag of B, or "likely".

Given that redshift, the image appears in rest frame of approximately 240 nm, which tracks objects with temperature ∼12,000 K such as hot, young stars and supernova remnants.

GZ5001 was imaged through the F160W filter by the Wide Field Camera 3 (WFC3) aboard HST. Dawson et al. (2001) measured a spectroscopic redshift of 2.011. Dawson et al.

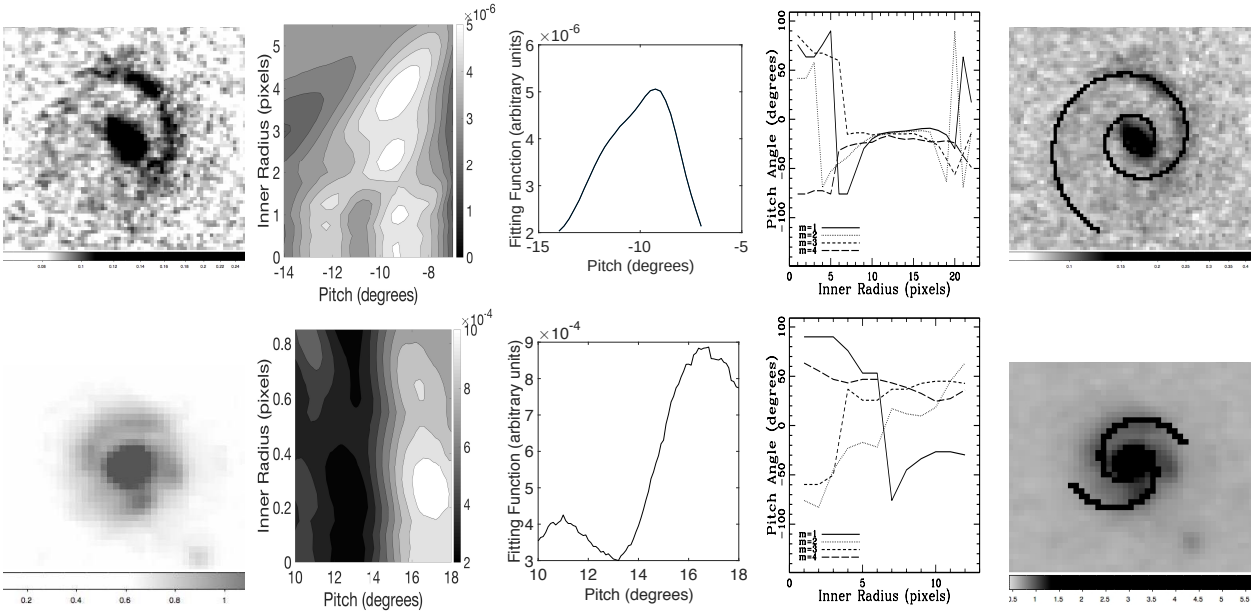

Figure 3.1: **Top row:** the redshift 2.3219 galaxy GS21 at J2000 right ascension 53.14863° and declination -27.95469°, with pitch angle $-9.08° \pm 2.08°$ as measured by Spirality and $-11.65° \pm 2.58°$ as measured by 2DFFT, with the negative sign denoting Z-winding. **Bottom row:** the redshift 2.011 galaxy GZ5001 at J2000 right ascension 189.14811° and declination 62.24002°, with pitch angle $16.59° \pm 2.78°$ as measured by Spirality and $14.27° \pm 6.55°$ as measured by 2DFFT. **Columns, from left to right: (1)** The image on which pitch angle analysis was performed; **(2)** Spirality's fitting function plotted against both pitch angle and the inner radius of the measurement annulus, with the galaxy's pitch denoted by vertical structures on the graph; **(3)** Spirality's fitting function as a function of pitch angle with a fixed inner radius (note that each graph in Column 3 is a cross section of the graph to its immediate left); **(4)** 2DFFT analysis, with pitch angle as a function of the inner radius of the measurement annulus, where the outer radius is held constant; **(5)** The original image, overlaid by the logarithmic spiral that was fit to the galaxy by Spirality.

(2003) performed followup spectroscopy and classified the galaxy as a hard X-ray source indicative of a buried Type II AGN.

Given that redshift, the image appears in rest frame of approximately 530 nm, which tracks Sunlike stars.

3.1 Methods

Galaxy arms are often modeled as logarithmic spirals - in polar coordinates, $r = r_0 e^{\theta \tan(\phi)}$. The pitch angle of the spiral, ϕ, is the angle between a line tangent to the spiral and the radial line at any point on the spiral. Thus pitch angle can vary from 0° (a perfect circle) to 90° (a ray).

In order to overcome the uncertainties inherent in low-resolution images, we estimated the pitch angle of each galaxy using three independent methods, and rejected galaxies for which the methods disagree. First, we fit the spiral arms to logarithmic spirals of known pitch using the Spirality software package. Then we used a variable inner radius two-dimensional Fourier analysis (2DFFT), as described in Davis et al. (2012). If those two methods yielded a consistent pitch, we overlaid a logarithmic spiral with the resulting pitch onto the spiral arms for visual comparison.

3.1.1 Deprojection

The measurement of pitch involves first deprojecting the galaxy to a face-on orientation. We assumed 36 different combinations of position angles and inclination angles for each object, and deprojected the image accordingly. Then we ran each deprojected image plus the unaltered image through a Fourier transform. We used 2DFFT to decompose spiral arms into a superposition of logarithmic spirals of different pitch angles and number of arms. Since the correct deprojection will result in logarithmic spiral arms, we then choose the most stable measurement from the 2DFFT output.

3.1.2 Spirality

We developed Spirality, a template fitting algorithm in which spiral arms are fit to a set of spiral coordinate systems (templates) with known pitch angles.

The Cartesian pixel coordinates are recorded along each spiral axis. We establish a set of evenly spaced points along the first spiral axis for the purpose of recording pixel values. The axis points are spaced sufficiently close together so that a single pixel may be recorded several times. The longer the path of the axis through a given pixel, the more times the pixel is counted. The mean pixel value along the axis points is then recorded. Figure 2.1 illustrates the process of finding the mean pixel value along a given spiral axis.

The process is repeated for the remaining axes. The number of axes is approximately $4\pi R$, where R is the galaxy radius in pixels, so that the pixels at the outer edge of the measurement annulus get read, on average, twice. Once the mean pixel value for each spiral axis is recorded in the first template, the variance of these means is computed. This is the fitting function. Its value is assigned to the pitch angle of the template. The process is then repeated for templates of many different pitches, resulting in the fitting function vs. template pitch angle.

If the code is measuring a synthetic spiral or a particularly clean galaxy image, the fitting function shows a global maximum at the spiral's true pitch. However, the presence of even a single foreground star can produce a monotonically increasing background in the fitting function. The true pitch may therefore produce a local maximum, with the global maximum occurring at the edge of the graph. Visual inspection of the graphs is therefore required.

A deeper discussion on Spirality is available in Shields et al. (2016), which available on the ArXiv.

3.1.2.1 Error Bars

Error bars are determined in a manner similar Davis et al. (2012). The pitch angle is measured on a series of annuli that are concentric with the galaxy. The outer radius is held constant, while the inner radius is varied. The fitting function now spans two independent variables: template pitch angle and inner radius.

A region of inner radii with reasonably constant pitch is identified by the user, and the standard deviation of the pitches in this region is computed. This number is scaled by the size of the stable radius segment relative to the radius of the galaxy. The result is added in quadrature with the measurement precision, or the number of degrees between consecutive template pitch angles. The error bar is output.

Because the error bar is larger if the logarithmic segment of the galaxy radius is smaller, the error bar is a first-order test of logarithmicity. If the user either overestimates or underestimates the length of the logarithmically stable radius segment, the error bar will suffer.

3.1.3 2DFFT and Spiral overlay

In addition to Spirality, the galaxies were analyzed using 2DFFT. An early version of this method is described in Saraiva Schroeder et al. (1994). An expanded version, which includes varying the inner radius in order to establish error bars, is described in Davis et al. (2012).

Finally, if Spirality and 2DFFT agreed on a pitch angle, we checked their result qualitatively by visual inspection. The deprojected galaxy image was overlaid by a logarithmic spiral with the pitch angle that was output by Spirality. We only included galaxies in this analysis for which Spirality, 2DFFT, and visual inspection all agreed on a pitch angle.

3.2 Results

Both galaxies showed apparent spiral structure. Visual inspection of GS21 shows one well-resolved spiral arm, with a kink between the bright inner part and the dim outer part. Visual inspection of GZ5001 shows a low-resolution system of two or possibly three arms, with a possible companion galaxy.

For GS21, Spirality measured a pitch angle of $-9.08° \pm 2.08°$, which is consistent with 2DFFT's measurement of $-11.65° \pm 2.58°$, where the negative sign denotes Z-winding. The weighted mean of the two measurements yields a pitch of $-10.1° \pm 1.6°$

For GZ5001, Spirality measured a pitch angle of $16.59° \pm 2.78°$, which is consistent with 2DFFT's measurement of $14.27° \pm 6.55°$ to within the error bars. The weighted mean of the two measurements yields a pitch of $16.2° \pm 2.6°$

In order to quantify the degree of consistency between Spirality's measurement and 2DFFT's measurement, we introduce the "difference factor" (D), which is the difference between the measurements divided by the sum of the uncertainties:

$$D = \frac{\phi_{Spirality} - \phi_{2DFFT}}{\Delta_{Spirality} + \Delta_{2DFFT}} \tag{3.1}$$

When Spirality's error bars overlap 2DFFT's, then $D < 1$ and the measurements are

consistent. When the error bars barely touch, $D = 1$. When the error bars do not overlap, $D > 1$.

GS21 showed a difference factor of 0.55, while GZ5001 showed a difference factor of 0.25. The low difference factors added to our confidence in the measurements, as did the spiral overlays. The results are summarized in Figure 3.1.

We also attempted to obtain a pitch angle measurement for the high-redshift galaxy obtained in Law et al. (2012). However, the difference factor for that galaxy was greater than unity. We therefore chose not to include the result.

3.3 Discussion

The measurements suggest that the high-redshift GS21 and GZ5001 may approximate logarithmic spirals, which is a common property among low-redshift galaxies. Elmegreen & Elmegreen (2014) suggests that spiral structure should be rare beyond $z \sim 2$.

Elmegreen et al. (2005) and Elmegreen et al. (2007) identify a few dozen spirals out of a few hundred $z > 2$ galaxies in the Hubble Ultra Deep Field. These classifications were based on the presence of a central clump and an exponential Sèrsic light profile, since spiral structure was typically not visible at $z > 2$. Elmegreen et al. (2007) points out that Sèrsic profiles very greatly for both spirals and ellipticals at high redshift, which makes Sèrsic index an uncertain indicator of morphological type at $z > 2$.

Law et al. (2012) and Dawson et al. (2003) each provided an example of a $z > 2$ spiral with visible arms, and we have provided an additional example.

Elmegreen & Elmegreen (2014) argue that spiral structure should only occur when the galaxy is dynamically cool. The galaxy in Law et al. (2012) showed spiral structure despite being dynamically hot. Their explanation was that the spiral structure was a transient effect sparked by a major merger. They suggested that the spiral structure should last no more than 100 Myr, which would explain the rarity of dynamically hot spirals.

A test to this claim can occur when kinematic data become available for GS21 and GZ5001. If these galaxies are dynamically hot, then perhaps the explanation given in Law et al. (2012) applies to these two galaxies as well. Indeed, the image of GZ5001 in Figure 3.1 does show a possible companion galaxy in the bottom right of the image, which might explain the single spiral arm. On the other hand, that would mean that we now have three examples of these transient spirals, which suggests they might not be as rare, or perhaps not as transient, as previously thought. Such a result would be explained if hot disks form spirals more readily than current simulations suggest.

If, on the other hand, GS21 and GZ5001 are dynamically cool, then spiral structure is no surprise. Elmegreen & Elmegreen (2014) suggests that galaxies should not be cool until after $z \sim 2$, so these counterexamples would raise the question of whether cool disks are more prevalent in this epoch than currently believed, and how they became cool at such an early epoch.

4 An Upper Limit on the Tightening of Galactic Spiral Arm Pitch Angle through Cosmic Time

We present a preliminary estimate of an upper limit of the tightening of spiral arm pitch angle in cosmic time since redshift $z \sim 1.5$, beyond which few of our data points lie. This redshift corresponds to a lookback time of apporoximately 9.5 billion years, assuming a flat universe composed of 69.11% dark energy with an expansion rate (Hubble Constant) of $67.74 \frac{km/s}{Mpc}$, values which are consistent with the updated results from Planck Collaboration et al. (2016).

4.1 Data Selection

We began with a sample of 203 visually selected spirals from the Version 2.0 data release of the Great Origins Observatories Deep Survey (GOODS) North and South fields Giavalisco et al. (2004), which covers approximately 320 square arcminutes in two fields. GOODS North is centered on the Hubble Deep Field North, while GOODS South is centered on the Chandra Deep Field South. The fields were chosen for their underabundance of foreground stars so that distant galaxies can be more easily imaged.

Our data comes from the 775-nm infrared band. The GOODS North exposure time was about 2.4 hours, while the GOOD South exposure time was about 2.0 hours. The spirals were visually selected.

4.1.1 Redshifts

In order to study evolution, we need to know each galaxy's redshift, which gives both its distance and the age of the Universe at the time we are viewing the Galaxy.

In general, there are two types of redshift measurements, photometric and spectroscopic. Photometric redshifts are estimated by measuring a galaxy's flux (apparent brightness) through several wavelength band filters, and fitting the combined result to a theoretical redshifted spectral energy distribution, which is a galaxy's relative brightness as a function of wavelength. The more filters are used, the more likely the correct fit will be found, but the method can occasionally yield spectacularly wrong results.

Where possible, we rejected photometric redshifts in favor of spectroscopic redshifts. Spectroscopic redshifts fit patterns of spectral lines to known patterns that can be measured in the laboratory. Spectroscopic redshifts are therefore generally considered more reliable than photometric. We obtained our redshifts from the SIMBAD astronomical database.

After rejecting galaxies for which redshifts were not available, we were left with 171 spectroscopic and 14 photometric redshifts.

4.1.2 Agreement of Independent Measurements

We first measured the pitch angle using 2DFFT, then again using Spirality. We chose to use two independent measurements because the angular radii of the galaxies ranged from 19 pixels to approximately 250, and the pixellation of the lowest-resolution images presented a challenge for both measurement codes. We therefore wanted to keep only those galaxies for which where was reasonable agreement between the two codes' measurements.

We quantified the extent to which the codes agreed by assigning each galaxy a Difference Factor D, which is ratio of the difference in the measurements to the sum of the uncertainties:

$$D = \left| \frac{\phi_{Sp} - \phi_{2D}}{\delta_{Sp} + \delta_{2D}} \right|, \tag{4.1}$$

where ϕ_{Sp} and ϕ_{2D} are a galaxy's pitch angle as measured respectively by Spirality and 2DFFT, and δ_{Sp} and δ_{2D} are their respective uncertainties. If $D < 1$, the error bars overlap and the measurements are unambiguously consistent. If $D = 1$, the error bars barely touch. If $D > 1$, the error bars to not overlap.

In considering which data points to reject from our sample, we also considered the extent to which each code individually had difficulty measuring the spiral, as quantified by the size of the error bars. We assigned each galaxy the quantity Δ, which is simply the larger of the two uncertainties.

In the balance between maintaining a large sample size and rejecting data for which we are not confident, we somewhat arbitrarily chose a maximum allowed error bar Δ_{max} of 8.0° and a maximum allowed disagreement factor D_{max} of 1.4. In other words, we rejected every galaxy for which either Spirality or 2DFFT quoted an error of more than 8.0°. We also rejected every galaxy for which Spirality and 2DFFT disagreed by more than 1.4 times the sum of their uncertainties.

After rejecting these data points, we were left with 85 galaxies. For each galaxy, we combined the Spirality and 2DFFT measurements weighing each code's measurement by the inverse square of its uncertainty and then taking the mean. The resulting pitch angle ϕ is

then given by

$$\phi = \frac{\frac{\phi_{Sp}}{\delta_{Sp}^2} + \frac{\phi_{2D}}{\delta_{2D}^2}}{\frac{1}{\delta_{Sp}^2} + \frac{1}{\delta_{2D}^2}} \tag{4.2}$$

which simplifies to

$$\phi = \frac{\phi_{Sp}\delta_{2D}^2 + \phi_{2D}\delta_{Sp}^2}{\delta_{Sp}^2 + \delta_{2D}^2}, \tag{4.3}$$

where ϕ_{Sp}, ϕ_{2D}, δ_{Sp}, and δ_{2D} are the the same variables as in Equation 4.1.

The uncertainties are treated as independent, and averaged by adding their inverses in quadrature and then taking the inverse of the result. The overall uncertainty δ, then, is given by

$$\delta = \frac{1}{\sqrt{\frac{1}{\delta_{Sp}^2} + \frac{1}{\delta_{2D}^2}}} \tag{4.4}$$

which simplifies to

$$\delta = \frac{\delta_{Sp}\delta_{2D}}{\sqrt{\delta_{Sp}^2 + \delta_{2D}^2}} \tag{4.5}$$

where δ_{Sp} and δ_{2D} are the same variables as in Equation 4.1.

4.1.3 Selection bias

Astronomers continue to be plagued by the fact that dim objects tend to outnumber bright objects, but bright objects are easier to see. Therefore, much astronomical data is biased toward bright objects. The problem is known as selection bias.

The methods of dealing with selection bias are statistical. One can give extra weight to a data points that belong to a population that is believed to be undercounted. Alternately, one can boost the population of undercounted objects by creating artificial data points,

known as Monte Carlo data points. These artificial data points have values that are randomly generated but which fit the same distribution as the values in the population to which they are being added.

In either case, the goal is to achieve a complete data set by matching the luminosity distribution of the data set to that of the population of galaxies being studied. This is not an easy task for any data set, but it is particularly problematic for ours because our galaxies span a wide range of redshifts, while the luminosity distribution of spiral galaxies is a function of redshift, wavelength, and likely pitch angle.

4.1.3.1 Absolute magnitudes

In order to give a first-order accounting of selection bias, we collected absolute magnitude (luminosity) data from the NASA/IPAC Extragalactic Database (NED). We chose to collect 551-nm V-band (green) magnitudes because they are the most widely available and this band lies within the range of rest frame emitted wavelengths of our galaxies.

It is helpful to recall that magnitudes are a logarithmic scale in which a difference of 1 magnitude signifies a luminosity ratio of approximately 2.512, a difference of 5 magnitudes equals a luminosity ratio of 100, and more luminous galaxies have smaller (*i.e.*, more negative) magnitudes.

Figure 4.1 shows the distribution of V-band magnitudes in our data set. The histogram is overlaid by a Type IV Pearson probability distribution function (PDF) that best fits the data. The PDF has been scaled to have the same area as the histogram.

The distribution is remarkably close to Gaussian, with a kurtosis ("pointiness") of 3.02, where a Gaussian kurtosis is defined to be 3. Our magnitudes have a standard deviation

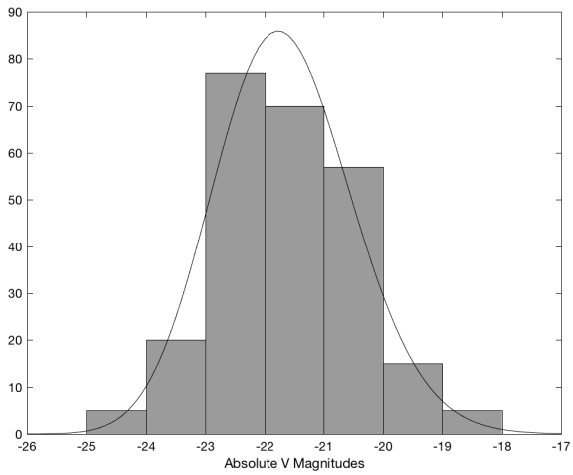

Figure 4.1: Distribution of absolute V-magnitudes for galaxies in our data set. The data show a mean of -21.6607, a standard deviation of 1.1565, a skewness of 0.1905, and kurtosis of 3.0245, where a Gaussian would have a kurtosis of 3.

of 1.15 about a mean of -21.67, and a skewness of 0.19. The small but positive skewness is graphically seen as a slight tail on the right side of the graph.

In contrast to our data set, the spiral luminosity function is by no means Gaussian. In a seminal paper on galaxy luminosity functions, Schechter (1976) points out that distant galaxies, whose visibility is limited by absolute magnitude, show an apparent luminosity function that appears more or less Gaussian. However, for galaxies in local clusters (where we expect to see dim galaxies as well as bright ones) the luminosity function at the bright end of the magnitude spectrum is best modeled as an exponential falloff and at the faint end by a power law. That is, the probability of finding a randomly selected galaxy within a faint luminosity bin depends on that bin's luminosity raised to some small, negative exponent which is generally called α.

Because magnitude is a logarithmic expression of luminosity, the power law at the

faint end of the spectrum would appear as a line with slope $-(1+\alpha)$ on a magnitude graph, where the slope may be slightly positive or slightly negative. For our data set, the value of α is unknown, but the difference between the theoretical slope $-(1+\alpha)$ on the right-hand (faint) side and the observed Gaussian falloff is the result of selection bias.

4.1.3.2 Three Data Sets

Because we have no way of accounting for the luminosity function across the full range of redshifts in our field, we chose to analyze our data in three ways:

1. First, we analyzed it as-is, with no accounting of selection bias.

2. Second, we analyzed a subset that only included the magnitudes near the mean. Specifically, we kept those galaxies such that $-23 \leq M_V \leq -20$, where M_V is the absolute V magnitude.

3. Finally, we added Monte Carlo data points to the near-the-mean subset so that the three remaining magnitude bins (23-22, 22-21, and 21-20) all had equal numbers of data points. This is admittedly a first-order attempt at dealing with selection bias in the absence of a measured luminosity function that spans the full range of redshifts in our data sets. However, assuming the luminosity function is a power law, it would behave by more or less flattening out immediately to the right of the bright-end cutoff, which is where our data set lies. If the Schechter exponent has value $\alpha = -1$ the graph would turn flat. If $\alpha > -1$ the slope would turn negative on the magnitude graph, and if $\alpha < -1$, the slope would turn positive.

Because the third data set takes selection bias into account, even if only in a first-order way (by assuming $\alpha = -1$), we have more confidence in the result from the third data set than from the results from the first two.

4.1.3.3 Monte Carlo Simulation

In order to simulate a complete sample of galaxies within a small range of absolute magnitudes (*i.e.*, luminosities) we chose to focus on the three central luminosity bins. We divided our data into magnitude bins, each of width 1 magnitude. This width was chosen because it was small enough to show the distribution curve but large enough to avoid the large variations that occur when each bin has too few data points.

The brightest 2 bins and the dimmest 2 bins were eliminated because they lacked a sufficient number of data points to be statistically viable. The 3 central bins were kept.

The bin ranging from magnitude -23 to -22 had the most data points. Therefore, no Monte Carlo points were added to this bin. Rather, Monte Carlo points were added to the bin ranging from -22 to -21, and to the bin ranging from -21 to -20, until all three bins had the same number of data points.

For each magnitude bin, we computed the means of the galaxies' pitch angles, pitch angle errors, and redshifts. We then computed the standard deviations, skewnesses, and kurtoses of these quantities. Using that information, we then computed the requisite number of Monte Carlo data points for each bin. Each Monte Carlo data point had a pitch angle that was randomly drawn from the Type IV Pearson probability distribution function (PDF) of pitch angles in that particular magnitude bin. Each Monte Carlo data point's pitch angle error and redshift were determined in a similar way. In the event that a Monte Carlo value

was physically impossible (for example, a negative error), that value was recomputed.

Table 4.1 shows the number of Monte Carlo points computed for each bin, and the Pearson PDF parameters from which each data point was drawn.

Magnitude Bin	−23 to −22	−22 to −21	−21 to −20
Number of galaxies	32	16	19
Number of Monte Carlo points	0	16	13
Total number of data points	32	32	32
Mean **pitch** (°)	24.43	26.13	22.41
Standard deviation of pitches (°)	8.16	8.85	8.64
Skewness of pitches	0.28	0.50	0.60
Kurtosis of pitches	2.65	2.01	2.92
Mean **pitch error** (°)	2.91	3.23	2.94
Standard deviation of pitch errors (°)	1.04	1.10	1.29
Skewness of pitch errors	-0.16	-0.26	0.00
Kurtosis of pitch errors	2.30	2.71	1.70
Mean **redshift**	0.87	0.74	0.77
Standard deviation of redshifts	0.33	0.25	0.48
Skewness of redshifts	0.80	-0.46	1.90
Kurtosis of redshifts	4.89	2.65	7.77

Table 4.1: Galaxy V-band absolute magnitude bins and the artificial (Monte Carlo) data points added to them. For each magnitude bin, Monte Carlo data points were added until all the bins had the same number of galaxies. Values for each Monte Carlo data point were randomly drawn from Pearson distributions appropriate to their respective bin.

Each of these values is the mean result of 10,000 Monte Carlo simulations.

In future work, a more sophisticated way to account for selection bias will be to run the nearby galaxies in our sample through an artificial redshifting simulation, and estimate the redshift at which the galaxy would no longer be visible in our data set or at which the measured pitch angle would no longer be consistent with the value measured locally. We expect that the cutoff redshift (the maximum viable distance) would be a function of luminosity and also of pitch angle, since tight spirals get blurred out at low resolution and loose spirals tend to have low luminosity. We would then choose a minimum luminosity, and

determine the maximum redshift for which all spirals above the minimum luminosity would be reliably measurable, and then reject galaxies beyond that redshift. That way, we would have a more or less complete volume-limited sample. That would give us a smaller cosmic time range for which to study evolution, but it would also increase our confidence in the result.

4.2 Analysis

A standard linear regression requires the assumption that the errors in the x-axis values (in this case, redshift) are negligible compared to the errors in the y-axis values (in this case, pitch angle). Since our pitch angle errors are $\sim 10\%$ of their respective pitch angles, while spectroscopic redshift errors (where published) are less than 1% of their their respective redshifts, we felt justified neglecting redshift errors and using a standard regression.

For each data set (that is, the whole data set, the central three magnitude bins, and the central bins with the Monte Carlo points), we computed the evolution of spiral arm pitch angle in cosmic time using a standard linear regression with each data point weighted by the inverse square of its pitch angle error bar.

Slopes, intercepts, their respective errors, and confidence intervals were computed from a straightforward technique given in *G.L. Squires, Practical Physics, 3rd. Ed.*, p. 44 and Appendix E.

It should be noted that we present our result in the form

$$P = (m \pm \Delta m)(z - z_{mean}) + (b \pm \Delta b) \tag{4.6}$$

where P is the average pitch angle in degrees as a function of redshift, m is the slope, Δm is the error in slope, z is the redshift, z_{mean} is the mean redshift in our data set, b is the mean intercept (that is, the value of P at z_{mean}), and Δb is the error in b. We choose this form of the equation because Δm and Δb are independent of each other. This is graphically evident by the fact that the hyperbolae formed by the confidence intervals is centered on the point $(z_{mean}, P(z_{mean}))$. In other words, the regression line "pivots" around this point.

We choose *not* to present our results in the simpler form

$$P = (m \pm \Delta m)(z) + (c \pm \Delta c) \tag{4.7}$$

where c is the y-intercept and Δc is its error. The error in the slope and the error in the y-intercept are not independent of one another and therefore should not be used in the same equation. Nonetheless, the y-intercept and its error are useful for understanding the result, so we compute them and present them in the result table.

4.2.1 Monte Carlo error

The effect of adding random data points to a data set introduces an additional error to the slope and the intercepts, which we call the Monte Carlo error. This error is independent of the error caused by the scatter about the regression line, which we call the regression error. Therefore, for each regression value (slope, y-intercept, mean intercept), we computed the total error by adding the Monte Carlo error in quadrature with the regression error.

For example, the total error Δm in the slope is given by

$$\Delta m = \sqrt{\Delta m^2_{regression} + \Delta m^2_{MonteCarlo}}, \tag{4.8}$$

where $\Delta m_{regression}$ is the mean regression error computed over 10,000 Monte Carlo simulations and $\Delta m_{MonteCarlo}$ is the standard deviation of those 10,000 regression errors.

The total errors in the y-intercept and in the mean intercept, respectively, were computed in a similar way.

4.3 Results

Our results are summarized in Table 4.2. Results from each of the three data sets are discussed in their respective subsections below.

	All magnitudes	$-23 \leq V_{abs} \leq -20$	$-23 \leq V_{abs} \leq -20$ plus Monte Carlo
N	85	67	96
z_{mean}	0.70	0.71	0.72
m	7.39	8.92	6.44
Δm	2.60	3.17	3.50
b	20.15	20.08	21.11
Δb	0.85	1.01	1.13
c	14.91	13.74	16.47
Δc	2.01	2.47	2.72

Table 4.2: Regression results from the pitch angle vs. redshift analysis for three data sets. **Columns: (1)** Quantity being computed. **(2)** Computation for all galaxies in our data set. **(3)** Only those galaxies whose absolute V magnitudes are between -23 and -20. **(4)** Same as column 3, but with the addition of artificial (Monte Carlo) data points that simulate a luminosity function where $\alpha = -1$ as a first-order accounting of selection bias. **Rows: (1)** Number of data points (including Monte Carlo). **(2)** Mean redshift of data points. **(3)** Slope of pitch vs. redshift, in degrees per unit redshift. A positive slope indicates a decreasing (tightening) average pitch angle with time. **(4)** Error in the slope. **(5)** Mean intercept, or the computed mean pitch angle at the mean redshift of our data set. **(6)** Total error in the mean intercept. **(7)** y-intercept, which represents the mean pitch angle in the current epoch. **(8)** Error in the y-intercept.

4.3.1 No selection bias

As this data set does not take selection bias into account, we have the least confidence in this result. We simply include it as a baseline for comparison. With a total of 85 data points, this data set conforms to the equation

$$P = (7.40 \pm 2.60)(z - 0.70) + (20.14 \pm 0.85) \tag{4.9}$$

where P is the average pitch angle in degrees as a function of redshift, $m = 7.40$ is the slope, $\Delta m = 2.60$ is the error in slope, z is the redshift, $z_{mean} = 0.70$ is the mean redshift in this data set, $b = 20.14$ is the mean intercept (that is, the value of P at z_{mean}), and $\Delta b = 0.85$ is the error in b. This data set shows a y-intercept of $(14.97 \pm 2.01)^\circ$.

This result is shown in the left panel of Figure 4.2.

If this represented physical evolution, it would imply that spiral arm pitch angles have, on average, tightened by at most 7.4° or so per unit redshift. It also implies a mean pitch angle of about 15° in the local Universe (as given by the y-intercept), which is somewhat tighter than the value of 21.44° found by Davis et al. (2014).

4.3.2 Central luminosity bins

This data set includes the galaxies with absolute V-band magnitudes between -23 and -20 and ignores those galaxies whose luminosities are outliers. It can be considered a zeroth order selection bias because it limits our data to galaxies within a slightly tighter range of luminosities than the general data set. It should be noted, however, the the luminosity ratio between the brightest galaxy (absolute V-magnitude -23) and the dimmest (-20) is

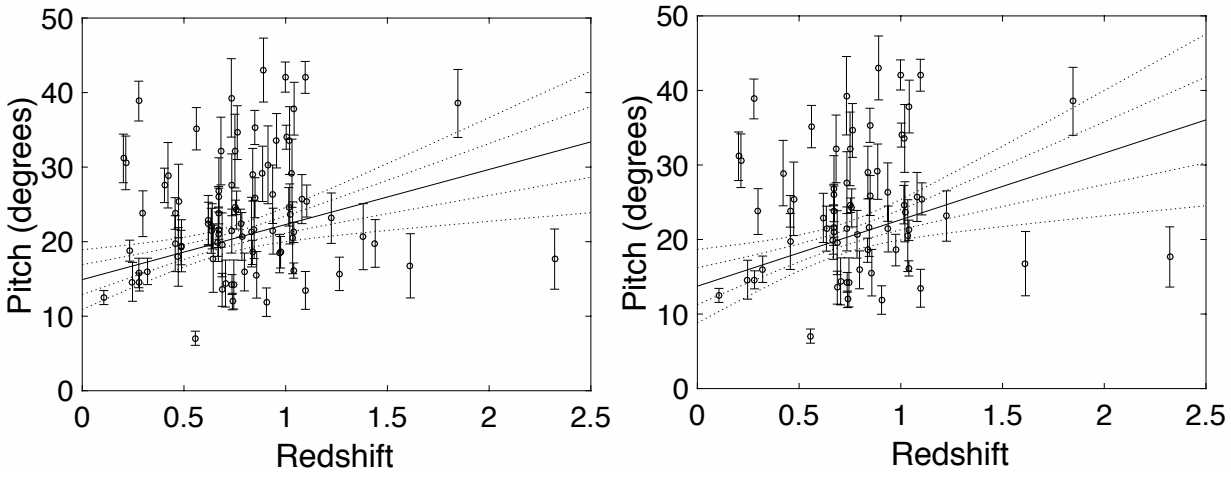

Figure 4.2: Pitch angle evolution in cosmic time for galaxies of all luminosities in our sample **(left)** and for galaxies with absolute V-band magnitudes between -23 and -20 **(right)**. The solid line is a standard linear regression. The inner set of dotted lines represent the 68% confidence interval for the regression line; the outer set represents the 95% confidence interval.

$100^{3/5}$, or slightly less than 16. Thus, the luminosities in these galaxies span slightly more than an order of magnitude.

With a total of 67 data points, this data set conforms to the equation

$$P = (8.92 \pm 3.17)(z - 0.71) + (20.08 \pm 1.01) \tag{4.10}$$

where the variables are defined the same was as in Equation 4.9. This data set shows a y-intercept of $(13.74 \pm 2.47)^\circ$.

If this represented physical evolution, it would imply that spiral arm pitch angles have, on average, tightened by at most 9° or so per unit redshift. It also implies a mean pitch angle of about 14° in the local Universe, which is tighter than the value of 21.44° found by Davis et al. (2014).

This result is shown in the right panel of Figure 4.2.

4.3.3 Selection bias

This data set includes Monte Carlo data points that equalize the number of galaxies in the absolute V-magnitude bins -23 to -22, -22 to -21, and -21 to -20. It can be considered a first accounting of selection bias because it assumes that the Schechter exponent α is equal to -1. While the actual value of α is unknown for our data set, -1 is well within the range of values for luminosity functions in general.

Because this data set takes selection bias into account, we believe this result is the most physical of the three. With 67 galaxies and an additional 29 Monte Carlo data points, this data set conforms to the equation

$$P = (6.44 \pm 3.50)(z - 0.72) + (21.11 \pm 1.13) \tag{4.11}$$

where the variables are defined the same was as in Equation 4.9. This data set shows a y-intercept of $(16.47 \pm 2.72)^\circ$.

This result implies that spiral arm pitch angles have, on average, tightened by at most 6° or so per unit redshift. It also implies a mean pitch angle of about 16° in the local Universe, which is tighter than the value of 21.44° found by Davis et al. (2014).

This result is shown in Figure 4.3.

Effect of Redshift on Pitch Angle Measurement

As photons travel through cosmic distances, their wavelengths are stretched as space itself expands. Thus, emitted light is redshifted (that is, shifted toward the low-energy end of the electromagnetic spectrum) by the time it reaches Earth. The more distant the galaxy,

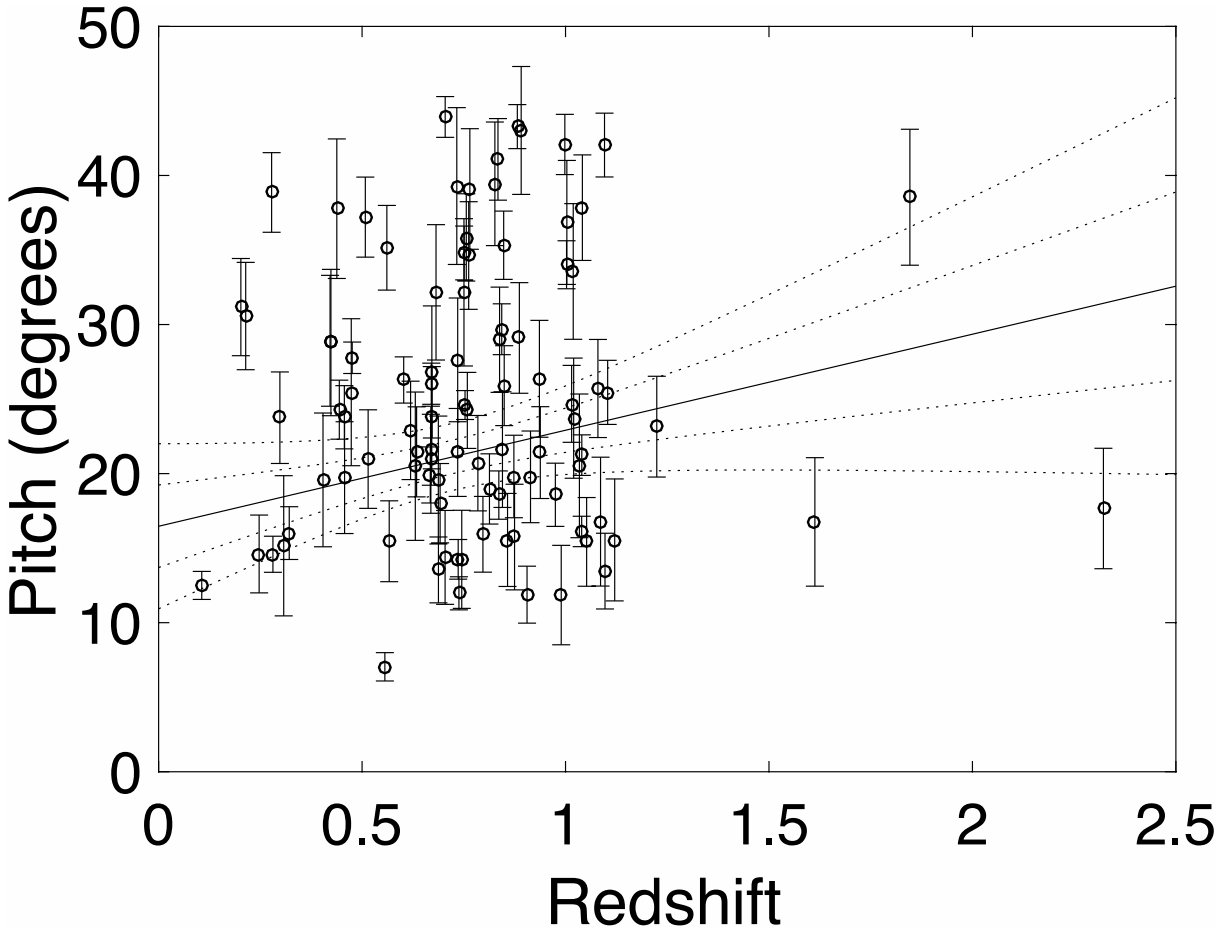

Figure 4.3: Pitch angle evolution in cosmic time for visually selected spirals in GOODS North and South with absolute V-band magnitudes between -23 and -20. Selection bias was accounted for by assuming a Schechter exponent of -1, which implies a flat luminosity function for this range of magnitudes. This was achieved by adding artificial (Monte Carlo) data points such that all luminosity bins had the same number of galaxies. The solid line is a standard linear regression. The inner set of dotted lines represent the 68% confidence interval for the regression line; the outer set represents the 95% confidence interval.

the more the light is redshifted, according to Hubble's Law. Thus, a photon passing through a telescope's filter was bluer when it was emitted (in its rest frame) than when detected. The emitted rest-frame wavelength λ_e of a photon emitted from a distance corresponding to redshift z is given by

$$\lambda_e = \frac{\lambda_o}{1+z}, \tag{4.12}$$

where λ_o is the observed wavelength. Thus, the more distant the galaxy, the bluer the rest frame wavelength.

The extent to which pitch angle depends on wavelength is becoming clearer as a result of recent work in our group. According to density wave theory, the spiral density wave triggers star formation, so ultraviolet light from the hottest, youngest, most massive, most luminous stars tracks the density wave itself. These stars have too short a lifetime ever to leave the density wave. Slightly older populations (blue stars, which live long enough to follow their orbital paths out of the density wave), should fall behind the spiral density wave outside the corotation radius but outpace the density wave inside the corotation radius. Thus the blue band should show a tighter pitch angle than the ultraviolet bands.

For redder stars the prediction of the density wave theory is debated, but observational results suggest that pitch angles measured throughout the visible spectrum and the near infrared do not vary much from those measured in the blue. For example, Seigar et al. (2006) used 2DFFT to establish a nearly one-to-one relationship (a slope of 0.98 $\pm$ 0.04) between blue band and near infrared band pitch angles for a sample of 66 galaxies. Moreover, Davis et al. (2012) used the variable inner radius 2DFFT method to remeasure 47 of the

galaxies from the Seigar et al. (2006) sample and also found a relation consistent with one-to-one, though with significant enough scatter to remain agnostic about density wave theory testing.

More recently, Pour-Imani et al. (2016) made a compelling case in support of the predictions of density wave theory. They used both 2DFFT and Spirality to measure 41 galaxies in four bands: 8 μm (mid infrared), which targets warm dust clouds in which stars form; 151 nm (far ultraviolet), which tracks extremely hot, extremely young (*e.g.*, B-type) stars in stellar nurseries; 445 nm (blue), which tracks slightly older (*e.g.*, F-type) stars; and 3.6 μm (mid infrared), which tracks old red stars. The 3.6 μm band does not correspond to the blackbody spectral peak of any star, but is particularly useful because most interstellar material is transparent to the 3.6 μm wavelength.

Pour-Imani et al. (2016) found that the 8 μm stellar womb and the 151 nm stellar nursery showed a one-to-one pitch angle correlation. The 445 nm stellar youths showed a systematically tighter pitch than the womb and the nursery. This result, combined with Seigar et al. (2006) and Davis et al. (2012), strongly supports the density wave theory, which affects the current project significantly.

In the GOODS sample, we measured the pitch angles of an initial sample of 203 spirals with redshifts ranging from effectively zero to 2.3219. Images were taken by Hubble Space Telescope's Advanced Camera for Surveys through the F775W filter, which passes 775-nm near infrared light. Our rest-frame emitted wavelengths, therefore, range from our observed near infrared wavelength down through the optical bands to 233 nm, which is in the ultraviolet.

Our near-infrared images track older stars, at least for galaxies in the local Universe. If the density wave theory is correct, then we do not expect that our pitch angle measurement would be affected at moderately high redshifts, so long as the rest frame emitted wavelength is in the near infrared or the non-blue optical bands. Indeed, Savchenko & Reshetnikov (2013) show a strong one-to-one correlation in pitch angles measured in the red band versus the visual (green) for a sample of 50 galaxies.

We do, however, expect pitch angle to be affected for galaxies at redshifts greater than $z \sim 0.78$, the distance at which the emitted rest frame wavelength is blue. Beyond that redshift, we are tracking young hot stars which should have a higher pitch angle than the older stars in a given galaxy. We therefore intuit that our pitch angles at high redshift are systematically too high, and therefore call our slope an upper limit.

It is worth noting that the evolution models that respectively give the best fits to all three of our data sets underestimate the average pitch angle of spiral galaxies locally, at redshift $z = 0$. The local mean pitch is about 21.4°, as measured by our group from a complete sample of local galaxies (see Davis et al. (2014) and Chapter 1 of this dissertation).

The amount by which the evolution models underestimate this value in each of the three calculations is comparable to the slope of each best-fit evolution curve. If there was little or no evolution, then the average pitch angle at redshift $z = 0$ (the local Universe) would be roughly the same as the average pitch angle at $z = 1$, which is easily computed by adding the slope to the y-intercept.

For all three of our data sets, the mean redshift at $z = 1$ is between 22° and 23° (See Table 4.2), which is more or less consistent with the local mean pitch of 21.4°. Thus,

a model without evolution would eliminate our need for an upper limit and give us a result consistent with the local pitch angle function, which is only known data point based on a complete sample (from the work of Davis et al. (2014)).

The work of Pour-Imani et al. (2016) suggests that there is a difference in pitch angle on the order of 5 degrees or more between the same galaxy imaged in the ultraviolet versus the optical or near infrared bands. This would be about the right amount we are looking for. Thus, the possibility exists that this effect pushes the best fit line upward on the high redshift end of the pitch angle-vs.-redshift graph. The complementary effect, then, is to the low redshift end of the best fit line down by a similar amount. Thus, our important observed effect from Pour-Imani et al. (2016) may explain the failure of the best fit line to agree with our results from Davis et al. (2014).

In other words, if we constrain our data to be consistent with the local pitch angle function, we find a result that is consistent with a non-evolving average pitch angle over cosmic time.

4.4 Conclusion

Our data, assuming galactic spiral arm pitch angle depends on emitted wavelength, places an upper limit on the tightening of the mean pitch angle over cosmic time as measured in optical and near infrared rest frame bands for galaxies with absolute V-band luminosities between -23 and -20. With 50% confidence, we find that the average pitch for such galaxies has decreased (tightened) by no more than 6.44 degrees per unit redshift. With 68% confidence, the upper limit is 9.94 degrees per unit redshift. With 95% confidence, it is

13.44 degrees per unit redshift.

We call this result an upper limit because our sample extends to redshifts at which the emitted wavelengths are in the ultraviolet bands, which have been demonstrated to show systematically higher pitch angles than the optical bands. The inclusion of these galaxies forces an artificial increase in the slope of the pitch angle vs. redshift relation (the rate of pitch angle decrease), as well as an artificial decrease in the y-intercept (the projected mean pitch in the local Universe).

If we constrain our data to be consistent with the local pitch angle mass function, we find a result that is consistent with a constant average pitch angle over cosmic time.

5 Dissertation Conclusion

We present Spirality, a novel method of measuring pitch angle by fitting the images to spiral templates of known pitch. Using this algorithm in concert with 2-dimensional Fast Fourier Transform (2DFFT), we determine that the redshift 2.011 galaxy GZ5001 (J2000 RA 189.14811°, Dec 62.24002°) has a pitch angle of approximately $16.2° \pm 2.6°$. The redshift 2.3219 galaxy GS21 (J2000 RA 53.14863°, Dec -27.95469°), which appears to be the most distant galaxy with visible spiral structure yet studied, has a pitch of approximately $-10.6° \pm 1.6°$.

Using a large sample of galaxies from the Great Observatories Origins Deep Survey (GOODS) and accounting for selection bias by assuming the Schechter exponent α is equal to -1, we place an upper limit on the tightening of average spiral arm pitch angle with cosmic time. With 50% confidence, we find that the average pitch for such galaxies has decreased (tightened) by no more than 6.44 degrees per unit redshift. With 68% confidence, the upper limit is 9.94 degrees per unit redshift.

If we constrain our data to be consistent with the local pitch angle mass function, we find a result that is consistent with a constant average pitch angle over cosmic time.

5.1 Status of Arkansas Galaxy Evolution Survey (AGES) Research

Since discovering the relationship between galactic spiral arm pitch angle and central black hole mass (Seigar et al., 2008; Berrier et al., 2013), the AGES group has contributed

to the body of knowledge in several ways:

1. We have further developed the 2DFFT method for measuring spiral arm pitch angle (Davis et al., 2012) and developed a novel method, Spirality (Shields et al., 2015), to serve as an independent check for high-redshift galaxies and other low-resolution galaxy images.

2. We have used our improved measurement techniques to establish the local pitch angle function and the local black hole mass function (Davis et al., 2014). This allows us to study both spiral structure and black hole mass using archival imaging without the need for spectroscopy.

3. We have shown that the Lin-Shu-Kalnajs dispersion relation holds for disk galaxies, forming a "fundamental plane" of spiral structure (Davis et al., 2015) in which pitch angle, central bulge mass, and gas density in the disk are all correlated. This supports the density wave theory, from which this dispersion relation derives.

4. We have shown that the pitch angle as measured in the far infrared (8 μm), and and the far ultraviolet (151 nm) is identical for a given galaxy (Pour-Imani et al., 2016). Pour-Imani (in prep) has shown that the pitch as measured from the H_α (656.28 nm) is identical to the 8 μm pitch and the 151 nm pitch. Furthermore, Pour-Imani et al. (2016) showed that the pitch angle measured throughout the optical and near infrared is largely identical, with at most a modest tightening at the infrared end of this range. However, the first complex (8 μm, Far UV, H_α) has a significantly looser pitch angle than the second complex (Optical, Near IR), by some 5 degrees or so. The 365 nm

U band tends to fall somewhere between these two complexes. This supports the density wave theory, which insists upon such a pitch angle difference between different wavebands.

5. We have begun the investigation of evolution of pitch angle with cosmic redshift, as discussed in this dissertation. The evidence to date places an upper limit on the amount of evolution, an upper limit which may become more tightly constrained soon.

Bibliography

Athanassoula, E., Romero-Gómez, M., Bosma, A., & Masdemont, J. J. 2009a, MNRAS, 400, 1706

Athanassoula, E., Romero-Gómez, M., Bosma, A., & Masdemont, J. J. 2010, MNRAS, 407, 1433

Athanassoula, E., Romero-Gómez, M., & Masdemont, J. J. 2009b, MNRAS, 394, 67

Balestra, I., Mainieri, V., Popesso, P., Dickinson, M., Nonino, M., Rosati, P., Teimoorinia, H., Vanzella, E., Cristiani, S., Cesarsky, C., Fosbury, R. A. E., Kuntschner, H., & Rettura, A. 2010, A&A, 512, A12

Beckwith, S. V. W., Stiavelli, M., Koekemoer, A. M., Caldwell, J. A. R., Ferguson, H. C., Hook, R., Lucas, R. A., Bergeron, L. E., Corbin, M., Jogee, S., Panagia, N., Robberto, M., Royle, P., Somerville, R. S., & Sosey, M. 2006, AJ, 132, 1729

Berrier, J. C., Davis, B. L., Kennefick, D., Kennefick, J. D., Seigar, M. S., Barrows, R. S., Hartley, M., Shields, D., Bentz, M. C., & Lacy, C. H. S. 2013, ApJ, 769, 132

Berrier, J. C. & Sellwood, J. A. 2015, ApJ, 799, 213

Bournaud, F. & Elmegreen, B. G. 2009, ApJ, 694, L158

Buta, R. 1989, in The World of Galaxies (Le Monde des Galaxies), ed. H. G. Corwin Jr. & L. Bottinelli (New York: Springer-Verlag), 29–44

Caldwell, J. A. R., McIntosh, D. H., Rix, H.-W., Barden, M., Beckwith, S. V. W., Bell, E. F., Borch, A., Heymans, C., Häußler, B., Jahnke, K., Jogee, S., Meisenheimer, K., Peng, C. Y., Sánchez, S. F., Somerville, R. S., Wisotzki, L., & Wolf, C. 2008, ApJS, 174, 136

D'Onghia, E. 2015, ApJ, 808, L8

Davis, B. L., Berrier, J. C., Johns, L., Shields, D. W., Hartley, M. T., Kennefick, D., Kennefick, J., Seigar, M. S., & Lacy, C. H. S. 2014, ApJ, 789, 124

Davis, B. L., Berrier, J. C., Shields, D. W., Kennefick, J., Kennefick, D., Seigar, M. S., Lacy, C. H. S., & Puerari, I. 2012, ApJS, 199, 33

Davis, B. L., Kennefick, D., Kennefick, J., Westfall, K. B., Shields, D. W., Flatman, R., Hartley, M. T., Berrier, J. C., Martinsson, T. P. K., & Swaters, R. A. 2015, ApJ, 802, L13

Davis, D. R. & Hayes, W. B. 2014, ApJ, 790, 87

Dawson, S., McCrady, N., Stern, D., Eckart, M. E., Spinrad, H., Liu, M. C., & Graham, J. R. 2003, AJ, 125, 1236

Dawson, S., Stern, D., Bunker, A. J., Spinrad, H., & Dey, A. 2001, AJ, 122, 598

de Vaucouleurs, G., de Vaucouleurs, A., Corwin, Jr., H. G., Buta, R. J., Paturel, G., & Fouqué, P. 1991, Third Reference Catalogue of Bright Galaxies. Volume I: Explanations and references. Volume II: Data for galaxies between 0^h and 12^h. Volume III: Data for galaxies between 12^h and 24^h.

Dekel, A., Sari, R., & Ceverino, D. 2009, ApJ, 703, 785

Elmegreen, B. G., Bournaud, F., & Elmegreen, D. M. 2008, ApJ, 688, 67

Elmegreen, D. M. & Elmegreen, B. G. 2014, ApJ, 781, 11

Elmegreen, D. M., Elmegreen, B. G., Ravindranath, S., & Coe, D. A. 2007, ApJ, 658, 763

Elmegreen, D. M., Elmegreen, B. G., Rubin, D. S., & Schaffer, M. A. 2005, ApJ, 631, 85

Giavalisco, M., Ferguson, H. C., Koekemoer, A. M., Dickinson, M., Alexander, D. M., Bauer, F. E., Bergeron, J., Biagetti, C., Brandt, W. N., Casertano, S., Cesarsky, C., Chatzichristou, E., Conselice, C., Cristiani, S., Da Costa, L., Dahlen, T., de Mello, D., Eisenhardt, P., Erben, T., Fall, S. M., Fassnacht, C., Fosbury, R., Fruchter, A., Gardner, J. P., Grogin, N., Hook, R. N., Hornschemeier, A. E., Idzi, R., Jogee, S., Kretchmer, C., Laidler, V., Lee, K. S., Livio, M., Lucas, R., Madau, P., Mobasher, B., Moustakas, L. A., Nonino, M., Padovani, P., Papovich, C., Park, Y., Ravindranath, S., Renzini, A., Richardson, M., Riess, A., Rosati, P., Schirmer, M., Schreier, E., Somerville, R. S., Spinrad, H., Stern, D., Stiavelli, M., Strolger, L., Urry, C. M., Vandame, B., Williams, R., & Wolf, C. 2004, ApJ, 600, L93

Gonzalez, R. A. & Graham, J. R. 1996, ApJ, 460, 651

Grogin, N. A., Kocevski, D. D., Faber, S. M., Ferguson, H. C., Koekemoer, A. M., Riess, A. G., Acquaviva, V., Alexander, D. M., Almaini, O., Ashby, M. L. N., Barden, M., Bell, E. F., Bournaud, F., Brown, T. M., Caputi, K. I., Casertano, S., Cassata, P., Castellano, M., Challis, P., Chary, R.-R., Cheung, E., Cirasuolo, M., Conselice, C. J., Roshan Cooray, A., Croton, D. J., Daddi, E., Dahlen, T., Davé, R., de Mello, D. F., Dekel, A., Dickinson, M., Dolch, T., Donley, J. L., Dunlop, J. S., Dutton, A. A., Elbaz, D., Fazio, G. G., Filippenko, A. V., Finkelstein, S. L., Fontana, A., Gardner, J. P., Garnavich, P. M., Gawiser, E., Giavalisco, M., Grazian, A., Guo, Y., Hathi, N. P., Häussler, B., Hopkins, P. F., Huang, J.-S., Huang, K.-H., Jha, S. W., Kartaltepe, J. S., Kirshner, R. P., Koo, D. C., Lai, K., Lee, K.-S., Li, W., Lotz, J. M., Lucas, R. A., Madau, P., McCarthy, P. J., McGrath, E. J., McIntosh, D. H., McLure, R. J., Mobasher, B., Moustakas, L. A., Mozena, M., Nandra, K., Newman, J. A., Niemi, S.-M., Noeske, K. G., Papovich, C. J., Pentericci, L., Pope,

A., Primack, J. R., Rajan, A., Ravindranath, S., Reddy, N. A., Renzini, A., Rix, H.-W., Robaina, A. R., Rodney, S. A., Rosario, D. J., Rosati, P., Salimbeni, S., Scarlata, C., Siana, B., Simard, L., Smidt, J., Somerville, R. S., Spinrad, H., Straughn, A. N., Strolger, L.-G., Telford, O., Teplitz, H. I., Trump, J. R., van der Wel, A., Villforth, C., Wechsler, R. H., Weiner, B. J., Wiklind, T., Wild, V., Wilson, G., Wuyts, S., Yan, H.-J., & Yun, M. S. 2011, ApJS, 197, 35

Grosbol, P. J. & Patsis, P. A. 1998, A&A, 336, 840

Guo, Y., Ferguson, H. C., Bell, E. F., Koo, D. C., Conselice, C. J., Giavalisco, M., Kassin, S., Lu, Y., Lucas, R., Mandelker, N., McIntosh, D. M., Primack, J. R., Ravindranath, S., Barro, G., Ceverino, D., Dekel, A., Faber, S. M., Fang, J. J., Koekemoer, A. M., Noeske, K., Rafelski, M., & Straughn, A. 2015, ApJ, 800, 39

Ho, L. C., Li, Z.-Y., Barth, A. J., Seigar, M. S., & Peng, C. Y. 2011, ApJS, 197, 21

Kendall, S., Kennicutt, R. C., & Clarke, C. 2011, MNRAS, 414, 538

Kennicutt, Jr., R. C. 1981, AJ, 86, 1847

Kermack, K. A. & Haldane, J. B. S. 1950, Biometrika, 37, pp. 30

Koekemoer, A. M., Faber, S. M., Ferguson, H. C., Grogin, N. A., Kocevski, D. D., Koo, D. C., Lai, K., Lotz, J. M., Lucas, R. A., McGrath, E. J., Ogaz, S., Rajan, A., Riess, A. G., Rodney, S. A., Strolger, L., Casertano, S., Castellano, M., Dahlen, T., Dickinson, M., Dolch, T., Fontana, A., Giavalisco, M., Grazian, A., Guo, Y., Hathi, N. P., Huang, K.-H., van der Wel, A., Yan, H.-J., Acquaviva, V., Alexander, D. M., Almaini, O., Ashby, M. L. N., Barden, M., Bell, E. F., Bournaud, F., Brown, T. M., Caputi, K. I., Cassata, P., Challis, P. J., Chary, R.-R., Cheung, E., Cirasuolo, M., Conselice, C. J., Roshan Cooray, A., Croton, D. J., Daddi, E., Davé, R., de Mello, D. F., de Ravel, L., Dekel, A., Donley, J. L., Dunlop, J. S., Dutton, A. A., Elbaz, D., Fazio, G. G., Filippenko, A. V., Finkelstein, S. L., Frazer, C., Gardner, J. P., Garnavich, P. M., Gawiser, E., Gruetzbauch, R., Hartley, W. G., Häussler, B., Herrington, J., Hopkins, P. F., Huang, J.-S., Jha, S. W., Johnson, A., Kartaltepe, J. S., Khostovan, A. A., Kirshner, R. P., Lani, C., Lee, K.-S., Li, W., Madau, P., McCarthy, P. J., McIntosh, D. H., McLure, R. J., McPartland, C., Mobasher, B., Moreira, H., Mortlock, A., Moustakas, L. A., Mozena, M., Nandra, K., Newman, J. A., Nielsen, J. L., Niemi, S., Noeske, K. G., Papovich, C. J., Pentericci, L., Pope, A., Primack, J. R., Ravindranath, S., Reddy, N. A., Renzini, A., Rix, H.-W., Robaina, A. R., Rosario, D. J., Rosati, P., Salimbeni, S., Scarlata, C., Siana, B., Simard, L., Smidt, J., Snyder, D., Somerville, R. S., Spinrad, H., Straughn, A. N., Telford, O., Teplitz, H. I., Trump, J. R., Vargas, C., Villforth, C., Wagner, C. R., Wandro, P., Wechsler, R. H., Weiner, B. J., Wiklind, T., Wild, V., Wilson, G., Wuyts, S., & Yun, M. S. 2011, ApJS, 197, 36

Law, D. R., Shapley, A. E., Steidel, C. C., Reddy, N. A., Christensen, C. R., & Erb, D. K. 2012, Nature, 487, 338

Lin, C. C. & Shu, F. H. 1964, ApJ, 140, 646

Ma, J. 2001, Chinese Journal of Astronomy and Astrophysics, 1, 395

Martínez-García, E. E. 2012, ApJ, 744, 92

Martínez-García, E. E., Puerari, I., Rosales-Ortega, F. F., González-Lópezlira, R. A., Fuentes-Carrera, I., & Luna, A. 2014, ApJ, 793, L19

Martinsson, T. P. K., Verheijen, M. A. W., Westfall, K. B., Bershady, M. A., Andersen, D. R., & Swaters, R. A. 2013, A&A, 557, A131

Nilson, P. 1973, Uppsala general catalogue of galaxies

Planck Collaboration, Ade, P. A. R., Aghanim, N., Arnaud, M., Ashdown, M., Aumont, J., Baccigalupi, C., Banday, A. J., Barreiro, R. B., Bartlett, J. G., & et al. 2016, A&A, 594, A13

Pour-Imani, H., Kennefick, D., Kennefick, J., Davis, B. L., Shields, D. W., & Shameer Abdeen, M. 2016, ApJ, 827, L2

Press, W. H., Flannery, B. P., Teukolsky, S. A., & Vetterling, W. T. 1989, Numerical recipes in C. The Art of Scientific Computing, ed. Press, W. H., Flannery, B. P., Teukolsky, S. A., & Vetterling, W. T. (Cambridge: University Press.)

Puerari, I., Block, D. L., Elmegreen, B. G., Frogel, J. A., & Eskridge, P. B. 2000, A&A, 359, 932

Puerari, I., Elmegreen, B. G., & Block, D. L. 2014, AJ, 148, 133

Saraiva Schroeder, M. F., Pastoriza, M. G., Kepler, S. O., & Puerari, I. 1994, A&AS, 108, 41

Savchenko, S. S. & Reshetnikov, V. P. 2013, MNRAS, 436, 1074

Schechter, P. 1976, ApJ, 203, 297

Scoville, N., Aussel, H., Brusa, M., Capak, P., Carollo, C. M., Elvis, M., Giavalisco, M., Guzzo, L., Hasinger, G., Impey, C., Kneib, J.-P., LeFevre, O., Lilly, S. J., Mobasher, B., Renzini, A., Rich, R. M., Sanders, D. B., Schinnerer, E., Schminovich, D., Shopbell, P., Taniguchi, Y., & Tyson, N. D. 2007, ApJS, 172, 1

Seigar, M. S., Bullock, J. S., Barth, A. J., & Ho, L. C. 2006, ApJ, 645, 1012

Seigar, M. S. & James, P. A. 1998, MNRAS, 299, 685

Seigar, M. S., Kennefick, D., Kennefick, J., & Lacy, C. H. S. 2008, ApJ, 678, L93

Shields, D. W., Boe, B., Pfountz, C., Davis, B. L., Hartley, M., Pour Imani, H., Slade, Z., Kennefick, D., & Kennefick, J. 2015, ArXiv e-prints

Simmons, B. D., Lintott, C., Willett, K. W., Masters, K. L., Kartaltepe, J. S., Häußler, B., Kaviraj, S., Krawczyk, C., Kruk, S. J., McIntosh, D. H., Smethurst, R. J., Nichol, R. C., Scarlata, C., Schawinski, K., Conselice, C. J., Almaini, O., Ferguson, H. C., Fortson, L., Hartley, W., Kocevski, D., Koekemoer, A. M., Mortlock, A., Newman, J. A., Bamford, S. P., Grogin, N. A., Lucas, R. A., Hathi, N. P., McGrath, E., Peth, M., Pforr, J., Rizer, Z., Wuyts, S., Barro, G., Bell, E. F., Castellano, M., Dahlen, T., Dekel, A., Ownsworth, J., Faber, S. M., Finkelstein, S. L., Fontana, A., Galametz, A., Grützbauch, R., Koo, D., Lotz, J., Mobasher, B., Mozena, M., Salvato, M., & Wiklind, T. 2017, MNRAS, 464, 4420

Willett, K. W., Galloway, M. A., Bamford, S. P., Lintott, C. J., Masters, K. L., Scarlata, C., Simmons, B. D., Beck, M., Cardamone, C. N., Cheung, E., Edmondson, E. M., Fortson, L. F., Griffith, R. L., Häußler, B., Han, A., Hart, R., Melvin, T., Parrish, M., Schawinski, K., Smethurst, R. J., & Smith, A. M. 2017, MNRAS, 464, 4176

York, D. 1966, Canadian Journal of Physics, 44, 1079

Appendix: Vitae and Publications

VITÆ

2001	Bachelor of Science in Physics, University of Houston, Houston, Texas
2012	Master of Science in Physics, University of Arkansas, Fayetteville, Arkansas

PUBLICATIONS

(a) *Multistation Studies of the Simultaneous Occurrence Rate of Pc 3 Micropulsations and Magnetic Impulsive Events.* Shields, D. W., Bering, E. A., Alaniz, A., Mason, S. E. M., Guo, W., Arnoldy, R. L., Engebretson, M. J., Hughes, W. J., Murr, D. L., Lanzerotti, L. J., & Maclennan, C. G. 2003, Journal of Geophysical Research, 108, A6

(b) *Measurement of Galactic Logarithmic Spiral Arm Pitch Angle Using Two-Dimensional Fast Fourier Transform Decomposition.* Davis, B. L., Berrier, J. C., Shields, D. W., Kennefick, J., Kennefick, D., Seigar, M. S., Lacy, C. H. S., & Puerari, I. 2012, The Astrophysical Journal Supplement Series, 199, 33

(c) *Further Evidence for a Supermassive Black Hole Mass-Pitch Relation.* Berrier, J. C., Davis, B. L., Kennefick, D., Kennefick, J. Seigar, M. S., Barrows, R. S., Hartley, M. T., Shields, D. W., Bentz, M. C., & Lacy, C. H. S. 2013, The Astrophysical Journal, 769, 132

(d) *The Black Hole Mass Function Derived from Local Spiral Galaxies.* Davis, B. L., Berrier, J. C., Johns, L., Shields, D. W., Hartley, M. T., Kennefick, D., Kennefick, J., Seigar, M. S., & Lacy, C. H. S. 2014, The Astrophysical Journal, 789, 124

(e) *A Fundamental Plane of Spiral Structure in Disk Galaxies.* Davis, B. L., Kennefick, D., Kennefick, J., Westfall, K. B., Shields, D. W., Flatman, R., Hartley, M. T., Berrier, J. C., Martinsson, T. P. K., & Swaters, R. A. 2015, The Astrophysical Journal Letters, 802, L13

(f) *Spirality: A Novel Way to Measure Spiral Arm Pitch Angle.* Shields, D. W., Boe, B., Pfountz, C., Davis, B. L., Hartley, M. T., Pour Imani, H., Slade, Z., Kennefick, D., & Kennefick, J. 2015, ArXiv, 1511.06365

(g) *Strong Evidence for the Density-wave Theory of Spiral Structure in Disk Galaxies.* Pour Imani, H., Kennefick, D., Kennefick, J., Davis, B. L., Shields, D. W., & Abdeen, M. S. 2016, The Astrophysical Journal Letters, 827, L2

(h) *Pitch Angle Analysis of Galaxies with Spiral Structure Between Redshifts 2.0 and 2.4*. Shields, D. W., Schilling, A., Kennefick, D., & Kennefick, J. 2017, The Astronomical Journal, Submitted

(i) *An Upper Limit on the Tightening of Galactic Spiral Arm Pitch Angle Pitch in Cosmic Time*. Shields, D. W., Pour Imani, H., Boe, B., Pfountz, C., Davis, B. L., Hartley, M. T., Slade, Z., & Kennefick, D. 2017, in prep.